CSIRO
AUSTRALIA

Implementation of a Soil-Canopy Scheme into the CSIRO GCM — Regional Aspects of the Model Response

E.A. Kowalczyk, J.R. Garratt and P.B. Krummel

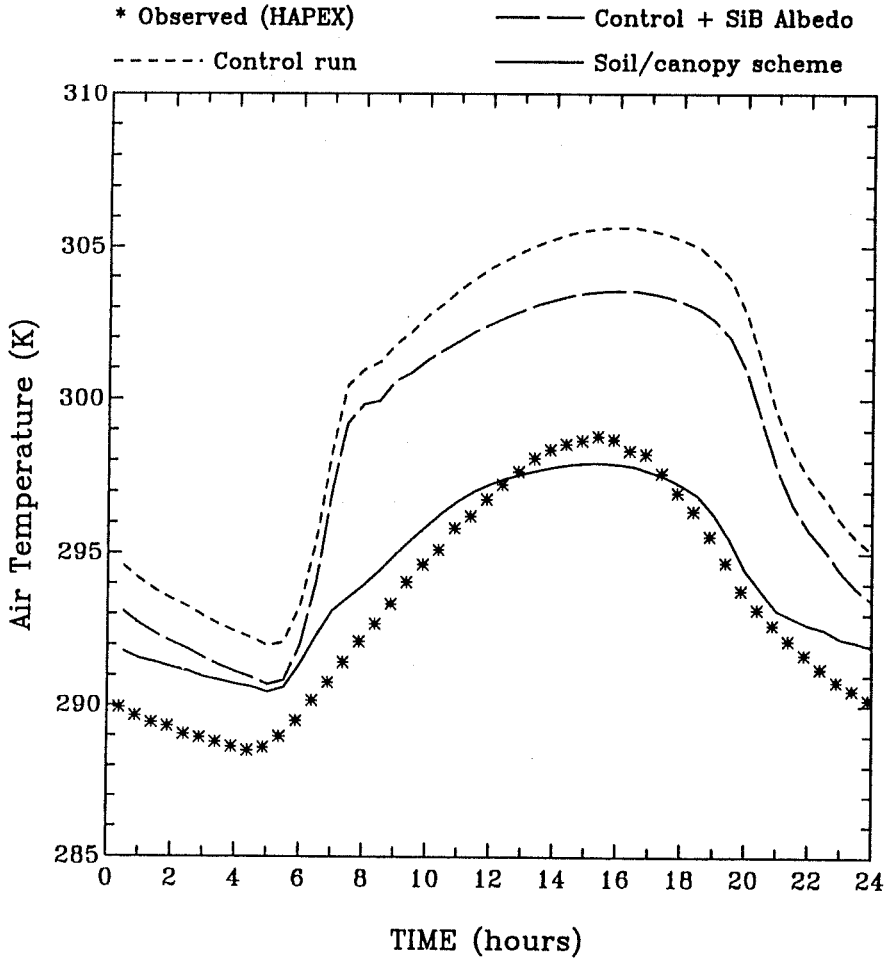

CSIRO Division of Atmospheric Research Technical Paper No. 32

CSIRO
AUSTRALIA

Implementation of a Soil-Canopy Scheme into the CSIRO GCM — Regional Aspects of the Model Response

E.A. Kowalczyk, J.R. Garratt and P.B. Krummel

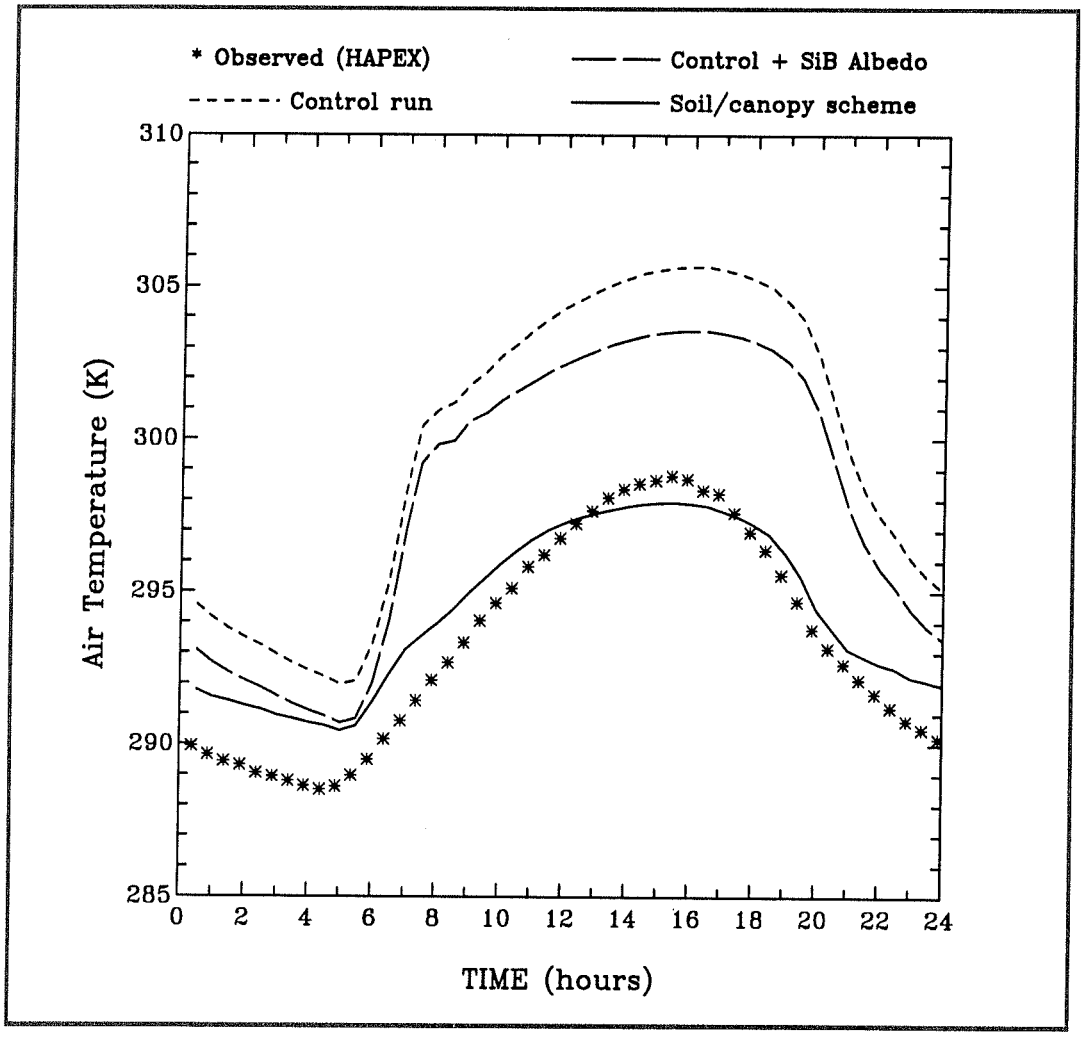

CSIRO Division of Atmospheric Research Technical Paper No. 32

National Library of Australia Cataloguing-in-Publication Entry

Kowalczyk, E. A. (Eva A.)
Implementation of a Soil-Canopy Scheme into the CSIRO GCM — Regional Aspects of the Model Response

Bibliography.
ISBN 0 643 05257 7.

1. Soil moisture - Mathematical models
2. Soil temperature -Mathematical models
3. Atmospheric circulation - Mathematical models
I. CSIRO Division of Atmospheric Research. II. Garratt, J. R. (John Roy). III. Krummel, P. B. (Paul B). IV. Title. (Series : CSIRO Division of Atmospheric Research technical paper ; no. 32).

631.43

©CSIRO Australia 1994

Printed on recycled, environmentally friendly paper

Implementation of a Soil-Canopy Scheme into the CSIRO GCM — Regional Aspects of the Model Response

E.A. Kowalczyk, J.R. Garratt and P.B. Krummel
CSIRO, Division of Atmospheric Research Private Bag 1, Mordialloc, Vic. 3195, Australia

Abstract

We have assessed the impact of a new soil-canopy scheme on aspects of the regional surface energy and water balances as simulated in the CSIRO 9-level GCM. Attention has been given to mean monthly statistics of rainfall, evaporation, soil moisture, net radiation and air temperature, both from a modelling and observational viewpoint. Five regions in Africa, Amazonia, Australia, Eurasia and north America were selected for study, with additional sites chosen for validation of the mean monthly diurnal cycle in air temperature, net radiation, sensible heat flux and evaporation simulated in the GCM. Each of these sites had comprehensive hourly observations of these quantities. Overall, we believe significant improvements to model simulations have resulted from implementation of the surface scheme discussed by Kowalczyk *et al.* (1991).

1 Introduction

Kowalczyk *et al.* (1991) described a soil-canopy scheme in the form of a 1D stand-alone model; the scheme is intended for use in numerical models of the atmosphere, specifically the CSIRO general circulation models (GCMs), limited area model (LAM) and Lagrangian atmospheric dispersion model (LADM). Its formulation, testing and implementation in the GCMs represented phase 1 of a long-term plan to improve the representation of ABL and surface processes in these models.

An important step in this phase of our work involved the systematic evaluation of the response of GCM simulations to the gradual introduction of each element of the soil-canopy scheme, and the quantification of the impact of the scheme upon climate properties (e.g. net radiation, evaporation, precipitation, soil moisture, near-surface air temperature) over the land surface. Such an approach is required if we are to understand the interaction between the surface scheme and other components of the numerical model.

The understanding of the behaviour of our own modelling systems has been aided (in the present context) by the study of Garratt (1994) and Garratt *et al.* (1993) who have evaluated the performance of several GCM systems through consideration of the regional surface energy balance and related observations.

We describe here the impact of the surface scheme on simulations in a low resolution version of the 9 - level GCM (CSIRO9). The impact is assessed by reference to the surface energy and water balances, and associated properties, both in terms of mean monthly values and mean monthly diurnal cycles. A 'zero-dimensional' ('0D') version of the scheme was implemented to allow testing in a mode decoupled from the GCM. Analyses of the '0D' model response to the presence of vegetation are assessed, as well as the sensitivity of the global and continental scale water balance components to changes in subgrid scale precipitation distribution.

2 Summary of Soil-Canopy Scheme

The scheme has a number of features similar to those described in Deardorff (1978) and Noilhan and Planton (1989). It allows for the inclusion of the following details - soil type (hence variable thermal and moisture properties); albedo; roughness length; canopy resistance; canopy interception of moisture; runoff; deep-soil percolation; snow accumulation and melting.

Subgrid scale processes are accounted for by regarding each land grid element as consisting of homogenous sub-cells of bare ground and vegetation. Calculation of surface temperature and fluxes are done separately for each sub-cell. Snow enters the calculation by modifying the thermal properties of the surface depending on the fractional snow depth, and modifying the albedo and roughness length. The scheme is described in Kowalczyk *et al.* (1991).

2a. Soil-canopy temperature and moisture, and surface fluxes

Soil temperature is calculated as in McGregor *et al.* (1993). There are three layers used, their thicknesses being chosen to enable a reasonable representation of both the diurnal and seasonal temperature waves through the soil (0.03, 0.255 and 2.5 m). The prognostic equations for the temperatures are

$$\frac{\partial T_g}{\partial t} = \frac{H_A - G_{12}}{\rho_s c_{s1} d_1}, \tag{1}$$

$$\frac{\partial T_{g2}}{\partial t} = \frac{G_{12} - G_{23}}{\rho_s c_{s2} d_2}, \tag{2}$$

$$\frac{\partial T_{g3}}{\partial t} = \frac{G_{23}}{\rho_s c_{s3} d_3}, \tag{3}$$

where ρ_s is the soil density, c_s is the soil specific heat (dependent on soil moisture and type), and d is a layer thickness. The last two parameters are evaluated for the snow/soil layer. G_{12} and G_{23} are the interlayer heat fluxes. H_A is given by the surface energy balance equation

$$H_A = (1-\alpha)R_{so}\downarrow + \epsilon_g R_{Lo}\downarrow - \epsilon_g \sigma T_g^4 - (H_g + \lambda E_g), \tag{4}$$

where $R_{so}\downarrow$ is the incoming solar radiation, $R_{Lo}\downarrow$ is the incoming long wave radiation, α is surface albedo, ϵ_g is the emissivity of the ground, σ is the Stefan-Boltzmann constant, and λ is the latent heat of vaporisation. The sensible heat flux H_g is calculated from

$$H_g = \rho_a c_p \frac{(T_g - T_a)}{r_{aH1}}, \tag{5}$$

where T_a is the air temperature, r_{aH1} is taken to be the aerodynamic resistance over a bare soil surface, ρ_a is the air density and c_p is the specific heat for air. λE_g is the latent heat flux from the ground, where

$$E_g = f(\frac{\eta_g}{\eta_{sat}}) E_l, \tag{6}$$

and is modelled as a fraction of the potential evaporation with a proportionality factor depending on the ratio of moisture at the surface (η_g) to the

saturation moisture (η_{sat}) and upon soil type. E_l is given by the Penman-Monteith combination equation (Garratt, 1992), written here as

$$\lambda E_l = \Gamma(R_N - G_o) + (1 - \Gamma)\rho\lambda\delta q_a / r_{aV1}, \tag{7}$$

where R_N is the net radiative flux density to the surface and G_o is the heat flux into the soil. Here $\Gamma = s/(s + \gamma)$, s is $\partial q^*/\partial T$, $\gamma = c_p/\lambda$ the psychrometric constant, $\delta q_a = q^*(T_a) - q_a$ is the humidity deficit in the air, and r_{aV1} is an aerodynamic resistance for bare soil. To account for snow, the roughness length varies linearly between 0.01 m for bare ground to 0.00024 m for ground covered with snow of depth 0.12 m or more.

In our scheme, the canopy is represented as a single vegetation layer with the characteristics of a large leaf acting as a source or sink of water vapour and sensible heat. The degree to which the canopy shields the ground from the solar radiation is characterized by the parameter σ_f, denoting the fraction of vegetation within a computational grid, and equal to 1 for complete blocking and to 0 for no foliage.

The canopy temperature T_f is obtained from the solution of the surface energy balance equation

$$(1 - \alpha_f)R_{so}\downarrow + \epsilon_f R_{Lo}\downarrow - \epsilon_f \sigma T_f^4 - H_f - \lambda E_f = 0, \tag{8}$$

where the sensible heat flux H_f is given by

$$H_f = \rho_a c_p \frac{(T_f - T_a)}{r_{aH2}}, \tag{9}$$

where r_{aH2} is the aerodynamic resistance for the canopy.

The water vapour flux over the grid area is assumed to arise from evaporation from the soil surface, E_g, and evaporation from the canopy E_f, itself comprising evaporation from the fraction of canopy covered with water, E_w (i.e. potential evaporation), and transpiration from the remaining part of the dry canopy E_{tr}. Evaporation from the wet canopy is given by

$$E_w = \rho_a \frac{(q^*(T_f) - q_a)}{r_{aV2}}, \tag{10}$$

where q^* is the saturation specific humidity at the foliage temperature. The resistance r_{aV2} is taken to be equal to r_{aH2}. Transpiration is parametrised as

$$E_{tr} = \rho_a \frac{(q^*(T_f) - q_a)}{r_{aV2} + r_s}, \tag{11}$$

where r_s is a bulk stomatal (surface) resistance. Again, to account for snow effects, the roughness length varies linearly between z_{0f} (roughness length for vegetation) to 0.01 m for vegetation covered with snow of depth $10z_{0f}$ or more.

The soil moisture contents are calculated from a moisture scheme for the combined canopy-soil surface layer

$$\frac{\partial \eta_g}{\partial t} = -C_1 \frac{(1-\sigma_f)E_g - ((1-\sigma_f)P\rho_w + \sigma_f P_g \rho_w + M_s \rho_{snow} - R\rho_w)}{\rho_w d_1'} - C_2 \frac{\eta_g - \eta_{eq}}{\tau}, \quad (12)$$

while the bulk layer moisture is given by

$$\frac{\partial \eta_2}{\partial t} = -\frac{\sigma_f(1-\beta)E_{tr}}{\rho_w d_2'} + \frac{d_1'}{d_2'}\frac{C_2}{C_1}\frac{(\eta_g - \eta_{eq})}{\tau}. \quad (13)$$

We have set $d_1' = 0.1$ m and $d_2' = 1$ m. In the above, ρ_w and ρ_{snow} are the densities of water and snow respectively. Note that evaporation occurs only from the fraction of grid with bare ground while the term $((1-\sigma_f)P\rho_w + \sigma_f P_g \rho_w + M_s \rho_{snow} - R\rho_w)$ represents the water flux reaching the ground, (P) is rainfall, (R) is runoff and (M_s) is snow melt. For bare ground $P_g = P$, and for a canopy, rain must first fill a reservoir of water on the canopy (m_c), so that

$$P_g = \begin{cases} 0 & \text{if } m_c < m_{c,max} \\ P & \text{if } m_c = m_{c,max}. \end{cases}$$

Details of the C_1 and C_2 coefficients and the definition of various terms can be found in Kowalczyk *et al.* (1991). Note that the equation for bulk moisture (13) contains a term (for $\sigma_f > 0$) describing the moisture uptake through the roots and its transport to the atmosphere through transpiration; the parameter β is defined by Eq.20, and is also taken as the fraction of the foliage covered with a film of water, depth m_c.

Finally, the combined soil-canopy temperature for a given GCM grid element is

$$T_{f,g} = (1-\sigma_f)T_g + \sigma_f T_f, \quad (14)$$

and the combined fluxes are

$$H_{f,g} = (1-\sigma_f)H_g + \sigma_f H_f \quad (15)$$

$$E_{f,g} = (1-\sigma_f)E_g + \sigma_f E_f, \quad (16)$$

where

$$E_f = (1 - \beta)E_{tr} + \beta E_w. \tag{17}$$

2b. Rainwater and dew interception

Rainfall and dew intercepted by the canopy are stored in a reservoir, of water content m_c. The equation for the water content of the reservoir (units of depth) is

$$\frac{\partial m_c}{\partial t} = P - \beta E_w/\rho_w, \tag{18}$$

where P is precipitation above the vegetation. The precipitation at the ground $P_g = P$ when m_c exceeds a critical value $m_{c,max}$, defined by Dickinson (1984) as

$$m_{c,max} = 0.2 \ max(LAI, 3.0), \tag{19}$$

where $m_{c,max}$ is the maximum depth (in mm) of the film of water that the vegetation can hold, and LAI is a leaf area index. E_w is the wet-surface evaporation or a dew deposition when the foliage temperature falls below the dew point of the air. β is set as a function of the depth of the interception reservoir defined by Deardorff (1978) as

$$\beta = \begin{cases} 1 & \text{if } condensation \\ m_c/m_{c,max} & \text{if } evapotranspiration. \end{cases} \tag{20}$$

2c. Stomatal resistance

In all canopy parametrisation schemes the stomatal resistance formulation plays a central role. The resistance depends on a range of factors including atmospheric conditions, availability of soil moisture, and vegetation type (e.g. Gates, 1980, chap. 10). The formulation used in the present scheme is based on Noilhan and Planton (1989), viz.

$$r_s = \frac{r_{si}^+}{LAI} F_1 F_2^{-1} F_3^{-1} F_4^{-1}, \tag{21}$$

where $r_s^+ = r_{si}^+/LAI$ is an unconstrained canopy (stomatal) resistance and is dependent on vegetation type. In the above, F_1 parametrises the effect of the radiation, F_2 describes availability of the water in the root zone for transpiration, F_3 represents the effect of vapour pressure deficit in the air and the function F_4 allows for a temperature dependence of the stomatal resistance with increasing value at high or low temperatures. See Kowalczyk *et al.* (1991) for details.

3 Observations - Climatological and Direct

3a. Climatologically Based

Henning (1989) gives maps of net radiation, sensible heat flux and evaporation for selected months for all the continents, whilst a global data set based on Willmott *et al.* (1985) provides monthly evaporation in grid point form at 1° intervals. Both sets are based on mean monthly values of reported station climatological variables recorded over many years (for the period 1931-60 in the case of Henning), and a range of empirical relations which relate the observed variables to the above three quantities. In the case of Henning, point values can be readily interpolated from the published maps, and regional estimates made by suitable summation over the desired areas. Values of the fluxes derived from these maps represent the most comprehensive data source for comparison with, and validation of, model-derived components of the surface energy balance (SEB). For the grid-point data, suitable averaging readily provides regional estimates of evaporation.

3b. 'Direct' Observations

3b1. SEB Components

Shuttleworth (1988) gives mean monthly values of the SEB component fluxes and precipitation for a two-year period at Manaus in Amazonia. This is the only known source of mean monthly values of all the component fluxes for such a long time period. Though net radiation values are based on direct observations for almost the complete two-year period, evaporation values are based on three short intensive observation periods whose information was used to calibrate a micrometeorological model of evaporation for the forest canopy. Similar observations, but for much shorter time periods, are available for other locations around the world (e.g. see Hicks, 1981 on the Wangara observations (Clarke *et al.*, 1971); HAPEX data (see André *et al.*, 1990); Amazonian data in Sato *et al.*, 1989). These observations can be used to derive the mean monthly diurnal cycle for single locations (and usually single months only).

3b2. Net Radiation

Kessler (1985; Table 17) provides mean monthly values of net radiation for a number of continental locations. The most reliable of these data utilise information for ten years or more and, in the latitude range between 70° N and 70° S, there are some 38 stations covering each month of the year (most stations are in Europe and the USSR, with only one station in the southern

hemisphere, at Aspendale near Melbourne, Australia). There is, of course (see above), the two-year Manaus data set which includes net radiation published by Shuttleworth (1988). Values of the net radiation from any number of these locations can be used to check interpolated values from Henning (1989) and model-generated values. For two of the sites found in the Kessler tabulations, Aspendale and Hamburg (see also Kasten, 1977 for the latter site), data for the individual years are available covering periods of ten and twenty years respectively. In addition, mean monthly values for a three-year period at a site near Boulder, Colorado are available, following Dutton (1990).

3b3. Precipitation and Screen air Temperature

Longterm observations of precipitation can be found in the data sets due to Jaeger (1976), Willmott *et al.* (1985) and in the World Climate Disc (1992), and screen temperature in the data set due to Legates and Willmott (1990) and in the World Climate Disc (1992).

The reliability of the observational data is discussed in Garratt *et al.* (1993).

4 Summary of GCM versions

The CSIRO9 atmospheric GCM is a spectral model using the flux form of the dynamical equations (Gordon, 1981). The flux, rather than advective form, ensures that conservation of mass and energy can be readily ensured. Details of the derivation of the equations and detailed description of the basic model as of 1992 is given by McGregor *et al.* (1993). The model has been coded for variable spectral (horizontal) resolution, which utilises an equally spaced East-West grid of 64 longitudes and an unevenly spaced Pole to Equator grid of 28 latitudes per hemisphere. R21 (rhomboidal truncation at 21 waves) is a standard resolution in this application. It uses the 'sigma' ($\sigma = p/p_*$) coordinate in the vertical with 9 levels. The main prognostic variables are the surface pressure p_*, the p_* weighted divergence $\hat{\mathrm{D}}$, vorticity $\hat{\zeta}$, temperature $\hat{\mathrm{T}}$ and moisture $\hat{\mathrm{q}}$. Horizontal diffusion is applied to divergence, vorticity, temperature and moisture fields. Model details include,

- annual and diurnal cycles,
- radiation code, based on the Schwartzkopf and Fels (1991) longwave radiation scheme and Lacis and Hansen (1974) shortwave radiation scheme,

- cloud cover diagnosed from the current state of the atmosphere (but is not directly coupled to the hydrological cycle),

- cloud scheme based on the Rikus (1990) adaptation of Slingo (1987) and extensively modified, see McGregor *et al.* (1993).

Other physical parametrisations included in the model are a mass flux cumulus convection scheme, shallow convection, gravity wave drag formulation and stability-dependent boundary layer. The surface fluxes of heat, moisture and momentum are parametrised following Monin-Obukhov similarity theory, with the model calculation of fluxes based on Louis (1979).

In the original version of the model, the fluxes from the land surface were calculated assuming constant surface roughness and soil radiative, thermal and hydraulic properties (except for the occurrence of snow), and no vegetation. Thus, a roughness length of $z_0 = 0.168$ m was set for all the land points. Land albedos were taken from Posey and Clapp (1964); evidence suggests that they are underestimated (see Table 1) in comparison with more recent data sets.

	AFRICA			**AMAZON**			**AUSTRALIA**		
Data Set	Jan	Jul	Year	Jan	Jul	Year	Jan	Jul	Year
SiB	0.260	0.249	0.255	0.137	0.144	0.139	0.259	0.269	0.264
Posey & Clapp			0.191			0.082			0.170
UKMO			0.255			0.130			0.243
UKMO (calc from model)	0.249	0.252	0.250	0.104	0.123	0.113	0.233	0.209	0.224
CSIRO9 from run E2	0.260	0.249	0.255	0.137	0.144	0.139	0.259	0.269	0.264
ERBE (Clear Sky)	0.294	0.281	0.291	0.152	0.165	0.158	0.204	0.213	0.210
GFDL Hi Res			0.297			0.143			0.201
	EURASIA			**NTH AMERICA**			**WEST SAHEL**		
Data Set	Jan	Jul	Year	Jan	Jul	Year	Jan	Jul	Year
SiB	0.197	0.187	0.189	0.179	0.154	0.166	0.200	0.174	0.185
Posey & Clapp			0.171			0.108			0.099
UKMO			0.187			0.172			0.168
UKMO (calc from model)	0.616	0.173	0.363	0.291	0.159	0.189	0.163	0.142	0.153
CSIRO9 from run E2	0.703	0.187	0.364	0.230	0.154	0.178	0.200	0.174	0.185
ERBE (Clear Sky)	0.609	0.191	0.326	0.206	0.167	0.183	0.193	0.170	0.187
GFDL Hi Res	0.539	0.186	0.329	0.319	0.174	0.211			0.194

Table 1: Albedo comparisons. See Table 2, Garratt *et al.* (1993).

The presence of vegetation influences properties of the surface such as albedo and roughness length. For example z_0 can vary from a low value of 1 mm over grass to 1 to 2 m for a tall forest, see Garratt (1993). Hence a new set of roughness data is used in the new version of the model incorporating the soil/canopy scheme. This scheme can be switched on/off through an input parameter. New data sets of fractional vegetation cover within a grid cell, unconstrained stomatal resistance, roughness length and albedo are based on Dorman and Sellers (1989), referred to as the SiB data sets. The last three properties are given on a monthly basis. In the new version of the CSIRO9 model, separate calculations of the bulk aerodynamic resistance over bare ground and over vegetation are performed for each grid cell containing vegetation; see Kowalczyk *et al.* (1991).

Three versions of the model were integrated to give minimum 5 year simulations. The first version, referred to as a control, uses the original surface scheme (McGregor *et al.* 1993); the control simulation is identified as C1. The second version is as C1 but uses the SiB set of albedos with the simulation identified as E1, and the third version is experimental, with the soil/canopy scheme switched on, and all data sets for surface specification included; the simulation is identified as E2.

5 Mean Monthly Statistics

In this study we assess GCM model performance by comparison of observed regional climates with model simulations. Emphasis is on surface, or near-surface, behaviour. Continental regions were chosen of area approximately 20° longitude and 15° latitude (20 GCM grid cells approximately) within Africa, Australia, Eurasia, South America and North America. Validation of regional climate is made using suitable observations of net radiation, evapotranspiration, precipitation and air temperature at the surface on a monthly time scale. Data are available in the form of monthly mean values and monthly mean diurnal cycles.

January and July results only are compared here, primarily because most observations are only available for these months. Simulations were performed with each of the three model versions. For each run, averages of a range of quantities over five to twelve years are used for comparison purposes. They are presented for each of the regions for January and July in Table 2.

JANUARY									
	Latent Heat Flux (Wm^{-2})					**Precipitation (mm/day)**			
Region	C1	E1	E2	Henn/Will	**Region**	C1	E1	E2	Jaeg/Will
Africa	15	11	15	0/2	Africa	0.36	0.28	0.17	0/0
Amazon	127	119	136	101/117	Amazon	8.88	8.09	6.90	9.9/9.9
Australia	47	38	51	54/59	Australia	2.70	1.79	1.62	2.1/3.1
Eurasia	4	4	4	-2/0	Eurasia	1.06	1.10	1.45	0.5/0.9
Nth America	29	27	24	12/3	Nth America	1.75	2.28	1.94	1.9/2.5
	Net Radiation (Wm^{-2})					**Sensible Heat Flux (Wm^{-2})**			
Region	C1	E1	E2	Henn	**Region**	C1	E1	E2	Henn
Africa	83	71	58	37	Africa	72	64	45	37
Amazon	148	137	141	123	Amazon	22	20	5	27
Australia	172	148	143	148	Australia	124	109	91	91
Eurasia	-13	-15	-15	-15	Eurasia	-7	-7	-10	3
Nth America	31	22	23	10	Nth America	10	3	5	11
	Longwave Radiation (Wm^{-2})					**Shortwave Radiation (Wm^{-2})**			
Region	C1	E1	E2		**Region**	C1	E1	E2	
Africa	109	107	125		Africa	192	178	182	
Amazon	45	44	39		Amazon	192	181	180	
Australia	109	111	117		Australia	281	259	260	
Eurasia	28	29	33		Eurasia	14	14	18	
Nth America	50	43	64		Nth America	82	65	87	
	Surface Temperature (K)					**Screen Temperature (K)**			
Region	C1	E1	E2		**Region**	C1	E1	E2	Will
Africa	292.8	290.9	292.7		Africa	292.5	290.8	291.4	292.9
Amazon	298.0	298.0	296.0		Amazon	297.9	297.8	296.0	298.2
Australia	305.2	303.2	303.8		Australia	303.6	301.9	301.3	302.0
Eurasia	257.1	258.1	262.7		Eurasia	257.6	258.7	262.8	256.4
Nth America	273.8	271.6	276.3		Nth America	274.2	272.0	275.5	274.2
	Bulk Moisture					**Surface Moisture**			
Region	C1	E1	E2		**Region**	C1	E1	E2	
Africa	0.085	0.070	0.070		Africa	0.057	0.054	0.068	
Amazon	0.280	0.273	0.340		Amazon	0.273	0.267	0.353	
Australia	0.115	0.111	0.076		Australia	0.092	0.085	0.077	
Eurasia	0.186	0.173	0.183		Eurasia	0.310	0.312	0.192	
Nth America	0.248	0.264	0.283		Nth America	0.285	0.307	0.288	

Table 2a: Summary of mean monthly regional statistics for January. Values based on observational data are shown (see Section 3) for Henning (Henn), Willmott (Will) and Jaeger (Jaeg).

JULY

	Latent Heat Flux (Wm^{-2})					**Precipitation (mm/day)**			
	Year					**Year**			
Region	C1	E1	E2	Henn/Will	**Region**	C1	E1	E2	Jaeg/Will
Africa	35	35	44	44/57	Africa	1.46	1.57	2.17	2.2/2.4
Amazon	48	44	91	63/81	Amazon	1.45	1.42	1.77	2.3/2.3
Australia	29	25	27	9041	Australia	1.16	1.20	0.98	0.5/0.3
Eurasia	45	47	80	50/64	Eurasia	0.98	1.16	2.03	1.5/1.7
Nth America	66	72	107	100/129	Nth America	2.78	3.19	3.94	2.9/3.3
	Net Radiation (Wm^{-2})					**Sensible Heat Flux (Wm^{-2})**			
Region	C1	E1	E2	Henn	**Region**	C1	E1	E2	Henn
Africa	133	122	117	120	Africa	99	87	72	88
Amazon	128	114	114	82	Amazon	80	70	23	23
Australia	65	53	45	29	Australia	40	32	21	24
Eurasia	138	131	141	128	Eurasia	82	74	57	67
Nth America	171	158	167	158	Nth America	100	82	57	
	Longwave Radiation (Wm^{-2})					**Shortwave Radiation (Wm^{-2})**			
Region	C1	E1	E2		**Region**	C1	E1	E2	
Africa	112	110	115		Africa	245	232	231	
Amazon	84	82	65		Amazon	212	179	180	
Australia	75	75	74		Australia	140	127	127	
Eurasia	120	115	101		Eurasia	258	247	242	
Nth America	95	90	79		Nth America	266	248	246	
	Surface Temperature (K)					**Screen Temperature (K)**			
Region	C1	E1	E2		**Region**	C1	E1	E2	Will
Africa	305.7	304.6	305.6		Africa	304.8	303.8	303.2	303.3
Amazon	299.4	298.5	295.0		Amazon	298.9	298.0	295.0	296.9
Australia	287.7	286.2	287.3		Australia	287.6	286.3	286.6	287.7
Eurasia	302.9	302.3	300.5		Eurasia	302.0	301.6	299.4	293.4
Nth America	305.3	303.6	300.5		Nth America	304.0	302.6	299.6	298.5
	Bulk Moisture					**Surface Moisture**			
Region	C1	E1	E2		**Region**	C1	E1	E2	
Africa	0.086	0.089	0.113		Africa	0.077	0.079	0.117	
Amazon	0.170	0.159	0.237		Amazon	0.124	0.125	0.240	
Australia	0.174	0.166	0.085		Australia	0.155	0.156	0.086	
Eurasia	0.156	0.155	0.160		Eurasia	0.080	0.086	0.161	
Nth America	0.166	0.175	0.279		Nth America	0.121	0.136	0.283	

Table 2b: Summary of mean monthly regional statistics for July. Values based on observational data are shown (see Section 3) for Henning (Henn), Willmott (Will) and Jaeger (Jaeg).

5a. Africa

The African region comprises an area belonging to the Sahara desert in the North and part of the subtropical area of the Sahel in the South. In the wet season, observed rainfall varies from about zero in the North to a high value of 6.2 mm day^{-1} in the South. In January, the observed level of net radiation at the surface is low at 37 W m^{-2}. In the control simulation (C1), see Fig. 1, an average net radiation of 83 W m^{-2} grossly overestimates this value. By increasing the albedo from $\alpha = 0.19$ to 0.26 in the first experimental simulation (E1), the net radiation is reduced to 71 W m^{-2}, and the inclusion of the soil/canopy scheme in the second experimental simulation (E2) reduces it further to 59 W m^{-2}. Very low evaporation in all three simulations agrees with observations and is closely related to the low precipitation and low soil moisture. The mean air temperature in simulations C1 and E2 is close to the observed value of 292.9 K, and is about 2 K lower in simulation E1.

In July the net radiation is reduced from 133 W m^{-2} in the control simulation to 122 W m^{-2} in simulation E1 and to 117 W m^{-2} in E2, which approximates well the observed value of 120 W m^{-2}, see Fig. 2. The decrease is mainly due to the albedo increase from $\alpha = 0.19$ to 0.25. The effect of the soil/canopy scheme on evaporation and precipitation is evident in the results of simulation E2. Evaporation and precipitation are increased from 35 W m^{-2} and 1.5 mm day^{-1} accordingly in simulations C1 and E1 to 47 W m^{-2} and 2.2 mm day^{-1} in E2. This compares well with the observed values of 44 W m^{-2} and 2.2 mm day^{-1}. Air temperature decreases from 304.8 K in the control simulation to 303.8 K in E1 and close to the observed value of 303.3 K in E2.

5b. South America

The region in South America comprises an area in the Amazon Basin. The level of net radiation in January is overestimated in the control simulation i.e. 148 W m^{-2} versus observed 123 W m^{-2}, see Fig. 3. Increased albedo from $\alpha = 0.08$ in simulation C1 to 0.137 in E1 and E2 slightly reduces it to about 140 W m^{-2}. The remaining difference is most likely due to uncertainties in the cloud scheme. Mean precipitation observed at 10 mm day^{-1}, is reduced from 8.9 mm day^{-1} in simulation C1 to 8.1 mm day^{-1} in E1 and to 6.8 mm day^{-1} in E2. Evaporation slightly increases in simulation E2 to 136 W m^{-2} and is higher than the observed range of 101 to 117 W m^{-2}. It tends to follow the behaviour of the net radiation as discussed in Garratt *et al.* (1993). Air temperatures in simulations C1 and E1 are close to the

observed 298.2 K, and are too low in E2, 296 K. Air temperature is closely related to surface temperature, see Garratt *et al.* (1993). This indicates that the outgoing thermal radiative flux is too low.

In July the net radiation is overestimated again, i.e. 128 W m^{-2} versus 82 W m^{-2}, see Fig. 4. The albedo, $\alpha = 0.082$, in simulation C1 is increased to 0.144 in E1 and E2. This reduces the net radiation slightly to about 114 W m^{-2}. Mean precipitation increases from 1.4 mm day^{-1} in simulations C1 and E1 to 1.9 mm day^{-1} in E2, closer to the observed value of 2.3 mm day^{-1}. Evaporation is underestimated in simulations C1 and E1 and overestimated in E2, i.e. 91 W m^{-2} compared with the observed range of 63 to 81 W m^{-2}. This is probably due to both increased precipitation and increased soil moisture. Air temperatures are close to the observed value of 298.2 K in simulations C1 and E1 and are underestimated by 3.2 K in E2. As with the January case, a lower surface temperature gives a lower outgoing longwave radiation.

5c. Australia

In January in Australia, the net radiation at the surface is overestimated by 24 W m^{-2}, see Fig. 5. The increase in albedo from $\alpha = 0.17$ in simulation C1 to 0.259 in E1 and E2 reduces it to the observed value of 148 W m^{-2} in simulation E1 and to 142 W m^{-2} in E2. Precipitation is reduced from 2.7 mm day^{-1} in simulation C1 to 1.8 mm day^{-1} in E1 and E2, which is close to the observed value of 2 mm day^{-1}. Evapotranspiration increases from 47 W m^{-2} in simulation C1 to 52 W m^{-2} in E2 which is close to the observed range of 54 to 59 W m^{-2}. Soil moisture is reduced from 0.11 to 0.08. A mean air temperature of 303.6 K in simulation C1 is reduced to 301.9 K in E1 and to 301.5 K in E2; the observed value is 302 K.

The effect of the albedo change and the introduction of the soil canopy scheme on July statistics is shown by a reduced level of net radiation from 65 W m^{-2} in simulation C1 to 53 W m^{-2} in E1 and to 45 W m^{-2} in E2, which remains above the observed level of 29 W m^{-2}, see Fig. 6. Precipitation is in the range 1.2 to 1.3 mm day^{-1} in all three simulations which exceeds the observed value of 0.5 mm day^{-1}. Evapotranspiration is in the range of 25 to 29 W m^{-2} and is close to the observed range of 10 to 24 W m^{-2}. Air temperatures are close to the observed value of 287.7 K for all simulations. Soil moisture has decreased from 0.17 in simulation C1 to 0.08 in E2, but with no evident effect on the simulated statistics.

5d. Eurasia

January statistics for Eurasia are not changed by the introduction of the new albedo and soil canopy scheme, see Fig. 7. This is due to snow cover and low temperatures. In conditions of low temperature i.e. about 258 K, evapotranspiration by vegetation is negligible. All the statistics are close to the observed values except air temperature which is several degrees too high.

In July, the net radiation in simulation C1 slightly overestimates the observed value i.e. 138 W m^{-2} versus 128 W m^{-2}, see Fig. 8. An increase in albedo from $\alpha = 0.171$ to 0.187 reduces it to 131 W m^{-2}, very close to the observed. However, inclusion of the soil/canopy scheme causes an increase in net radiation to 145 W m^{-2}. Precipitation is underestimated in simulations C1, 1.0 mm day^{-1}, and in E1, 1.2 mm day^{-1}, and is overestimated in E2 i.e. 2.2 mm day^{-1} versus an observed range of 1.5 to 1.7 mm day^{-1}. Increases in rain and soil moisture cause an increased evapotranspiration from about 46 W m^{-2} to 89 W m^{-2}, for an observed range of 50 to 64 W m^{-2}. Excessive air temperature in simulation C1, 302 K, and E1, 301.6 K, is reduced to 298.9 K in E2, still well above the observed value of 293.4 K.

5e. North America

January statistics for the USA region reveal excessive net radiation at the surface in simulation C1, 31 W m^{-2} versus the observed value of 10 W m^{-2}, see Fig. 9. An increase in albedo from $\alpha = 0.108$ to 0.179 in E1 reduces it to 22 W m^{-2}. Inclusion of the soil/canopy scheme increases this value slightly to 25 W m^{-2}. However the difference between simulated and observed values is within the $\pm$ 15 W m^{-2} reliability margin suggested by Garratt *et al.* (1993). Precipitation, evapotranspiration and soil moisture are similar in all simulations and are close to the observed values. The air temperature is equal to the observed value of 274.2 K in simulation C1, and is slightly underestimated in E1, and slightly overestimated in E2.

The July statistic for net radiation shows a slight overestimate, 171 W m^{-2}, versus the observed value of 158 W m^{-2}, see Fig. 10. An increase in albedo from $\alpha = 0.108$ to 0.154 in E1 reduces it to the observed value. Inclusion of the soil/canopy scheme increases the flux slightly to 169 W m^{-2}. Precipitation is increased from 2.8 mm day^{-1} in simulation C1 to 3.2 mm day^{-1} in E1 and to 3.8 mm day^{-1} in E2, which is outside of the observed range of 2.9 to 3.3 mm day^{-1}. This produces an increased evaporation from about 68 W m^{-2} in simulations C1 and E1 to 110 W m^{-2} which is in the observed range of 100 to 129 W m^{-2}. Air temperature decreases from 304 K in sim-

ulation C1 to 302.6 K in E1 and to 299.8 K in E2, which is close to the observed value of 298.5 K.

Summary

Overall, net radiation in the control simulation is overestimated in all the regions except Eurasia in January. This is common to all known GCM results, as discussed by Garratt *et al.* (1993). Use of the new (increased) albedos lowers the net radiation as would be expected. In the case of Australia in January, and Africa, Eurasia, and North America in July, it is reduced to close to the observed value. The main deficiencies in the simulation of net radiation are as stated by Garratt *et al.* (1993) and Garratt (1994):

- undervalued land albedo
- uncertainties in cloud scheme and clear sky absorption
- low surface temperature giving too low an outgoing longwave flux
- excessive incoming shortwave fluxes.

When the soil/canopy scheme is included, the mean monthly evapotranspiration increases in July in all the regions except Australia. This is mainly due to an increase in precipitation and soil moisture. Also, the presence of vegetation increases evapotranspiration due to extraction of water from the deep soil. In areas with significant vegetation cover, the air temperature falls, consistent with the increased evaporation.

Evapotranspiration in January is not changed significantly. This is mainly due to precipitation and soil moisture remaining unchanged in all regions except the Amazon Basin. In regions with either snow cover or too small a vegetation fraction the impact of the soil/canopy scheme on evaporation is insignificant. From a global perspective, Table 3 summarises observed precipitation and evaporation for all land within $\pm 60^0$ latitude, and the whole globe (land and ocean), with model values for the three simulations. Overall, land evaporation has increased with the inclusion of the full surface scheme, to a value in excess of the 'observed' value; this requires further investigation. Precipitation is little affected.

The present study indicates that, overall, the soil/canopy scheme, with attendant new data sets, provides an improved simulation of regional climate, with some deficiencies requiring further investigation.

	Precipitation (mm/day)			Evaporation (mm/day)		
Source	**Global**	**Land**	**Sea**	**Global**	**Land**	**Sea**
C1	2.963	0.701	2.262	2.975	0.429	2.546
E1	2.961	0.633	2.328	2.973	0.391	2.582
E2	3.059	0.687	2.372	3.071	0.500	2.571
Legates & Willmott 1992	3.118	0.638	2.479			
Budyko 1978	3.108	0.633	2.475	3.084	0.359	2.729
Albrecht 1961	2.608	0.568	2.041	2.608	0.349	2.259
Jaeger 1976	2.740	0.607	2.133			

Table 3: Simulated and observed/estimated values of precipitation and evaporation.

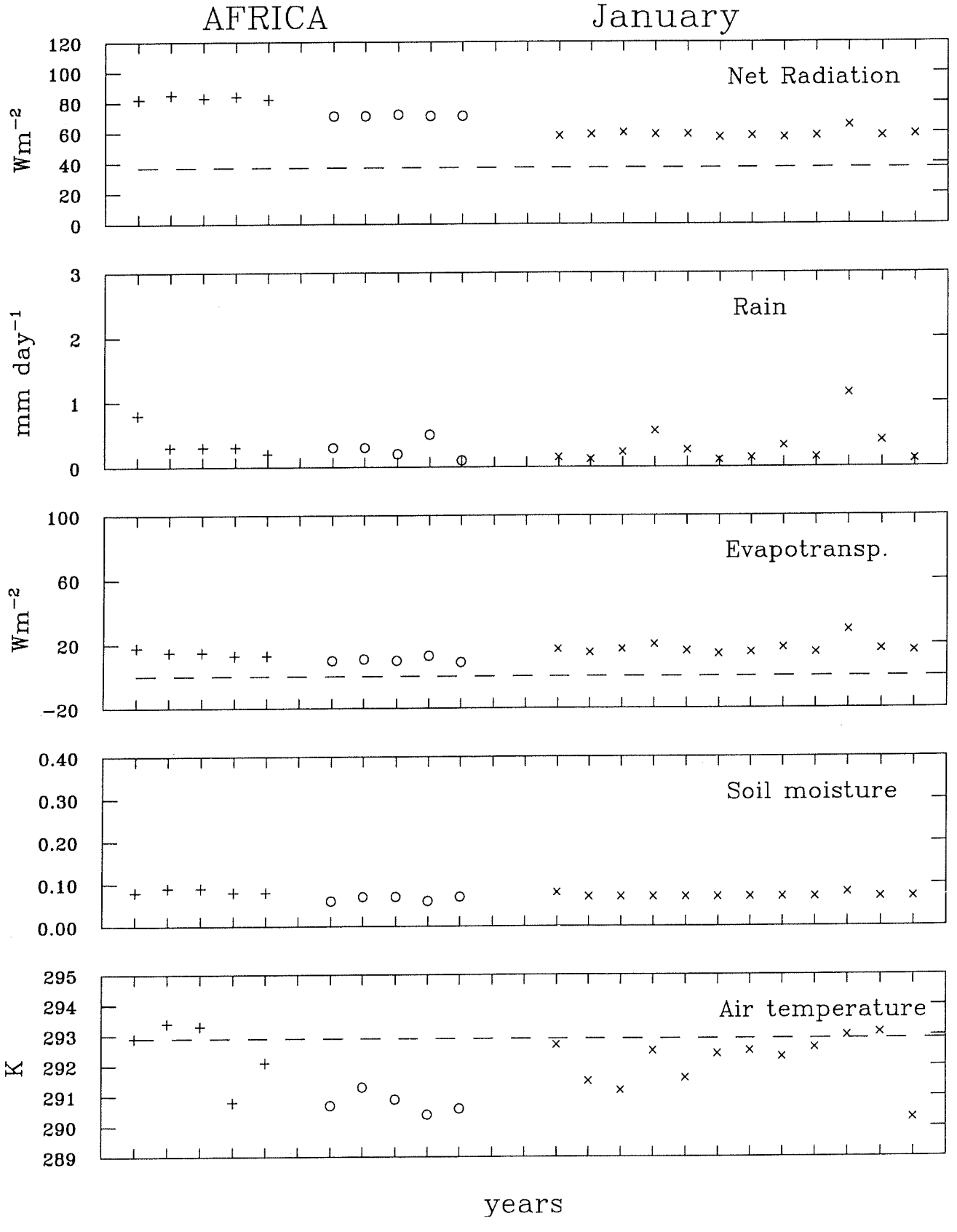

Figure 1: January means of net radiation, precipitation, evapotranspiration, soil moisture and air temperature for simulations: C1 '+', E1 'o' and E2 'x', for Africa. The dashed lines represent observed values.

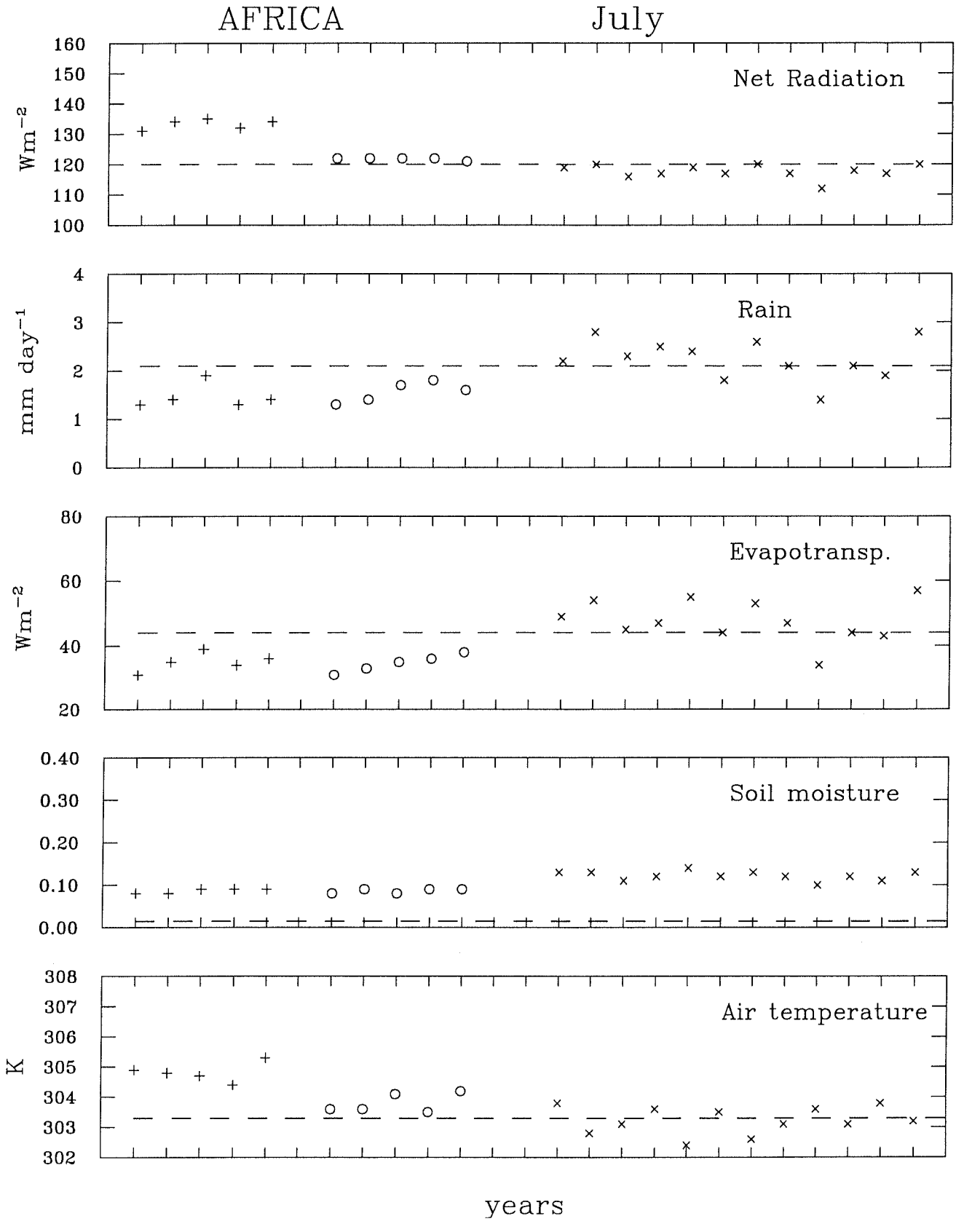

Figure 2: July means of net radiation, precipitation, evapotranspiration, soil moisture and air temperature for simulations: C1 '+', E1 'o' and E2 'x', for Africa.The dashed lines represent observed values.

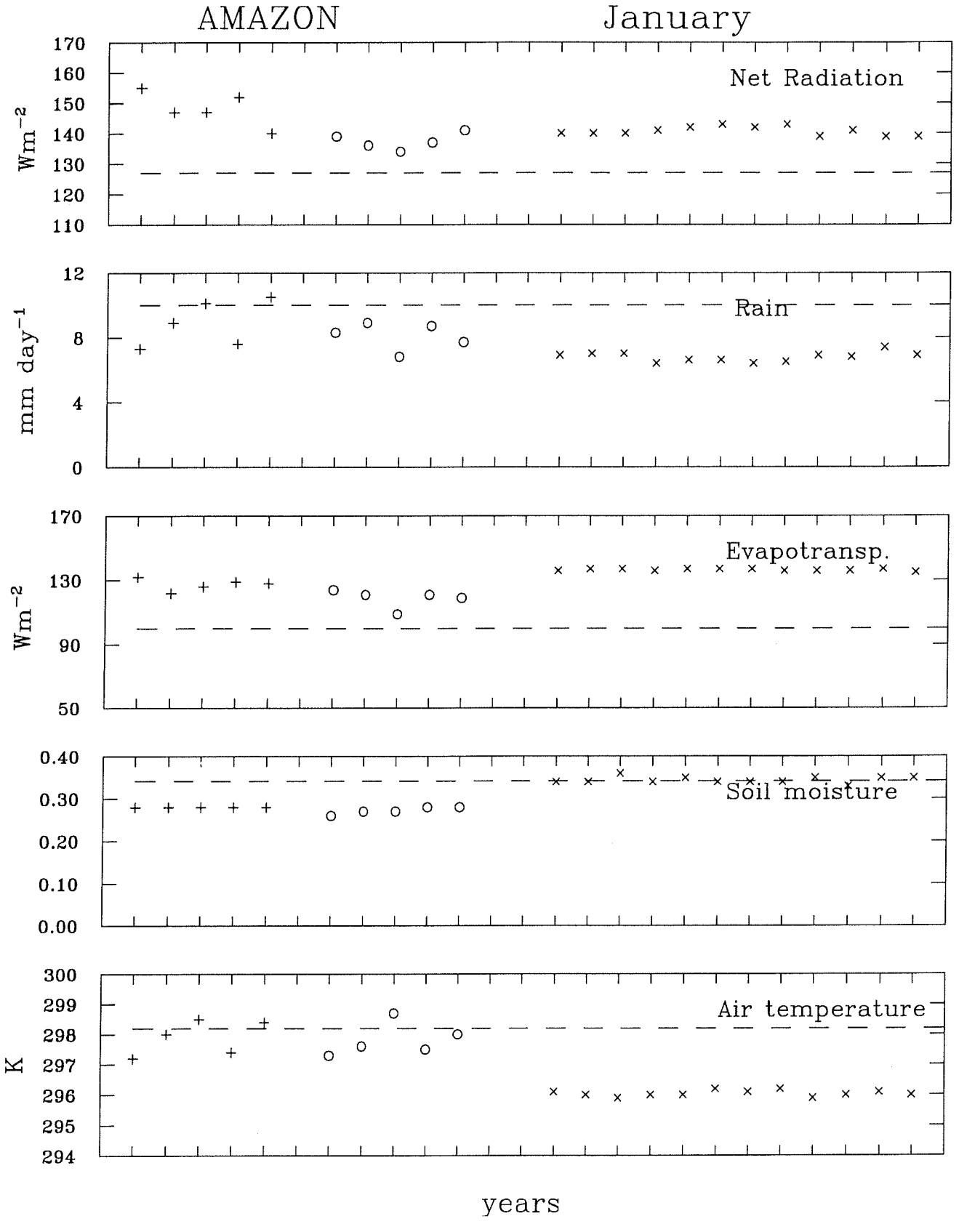

Figure 3: January means of net radiation, precipitation, evapotranspiration, soil moisture and air temperature for simulations: C1 '+', E1 'o' and E2 'x', for Amazon.The dashed lines represent observed values.

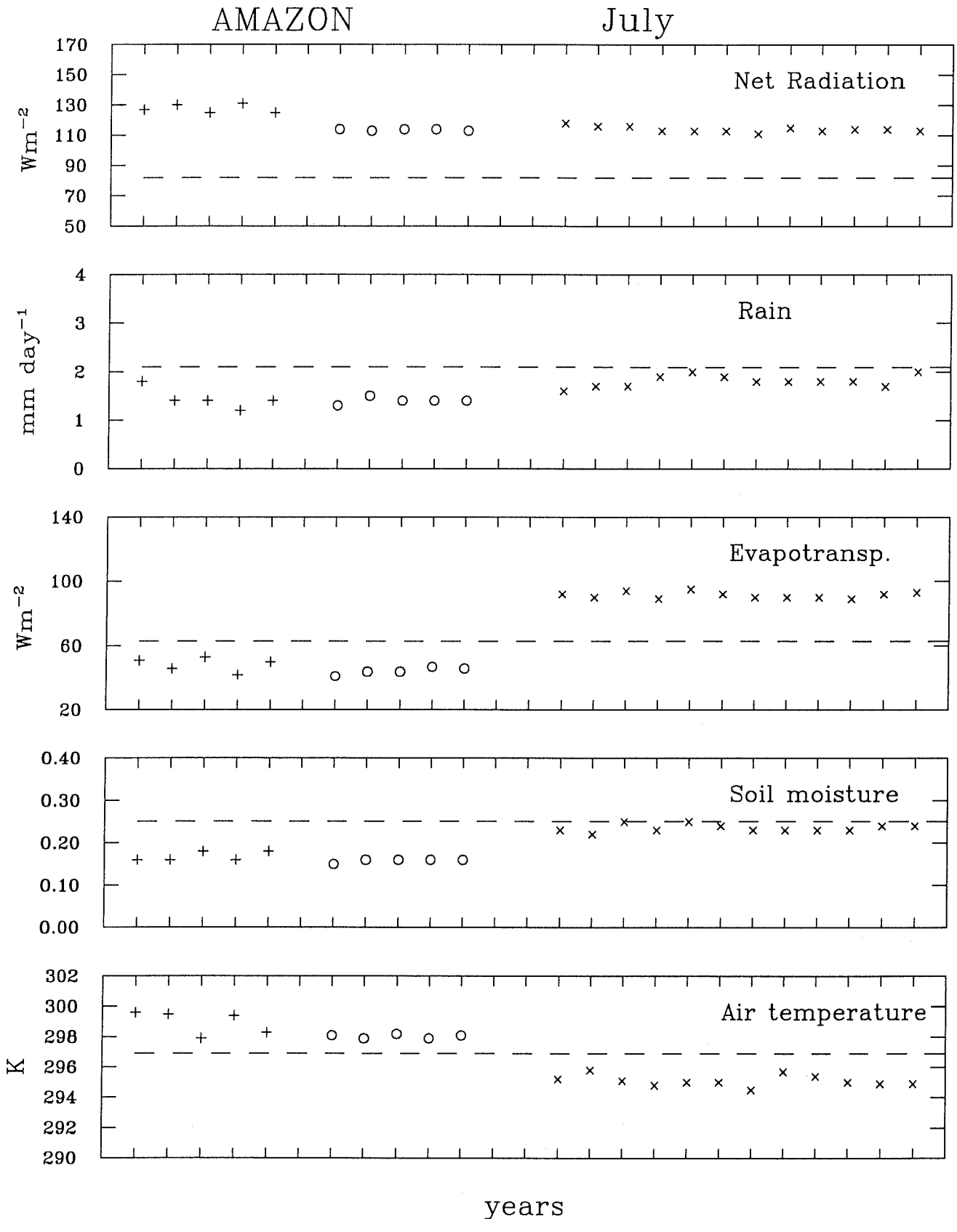

Figure 4: July means of net radiation, precipitation, evapotranspiration, soil moisture and air temperature for simulations: C1 '+', E1 'o' and E2 'x', for Amazon.The dashed lines represent observed values.

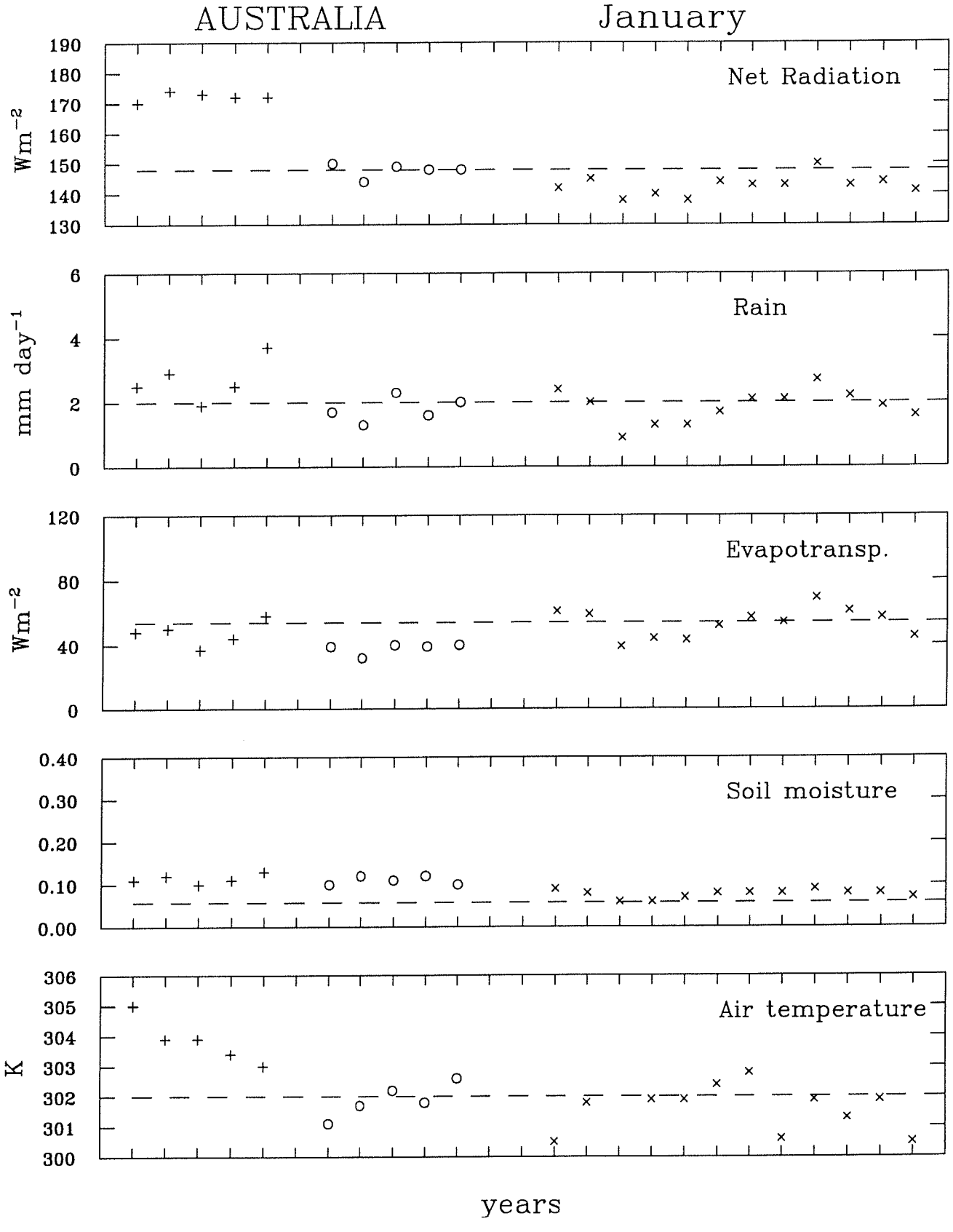

Figure 5: January means of net radiation, precipitation, evapotranspiration, soil moisture and air temperature for simulations: C1 '+', E1 'o' and E2 'x', for Australia. The dashed lines represent observed values.

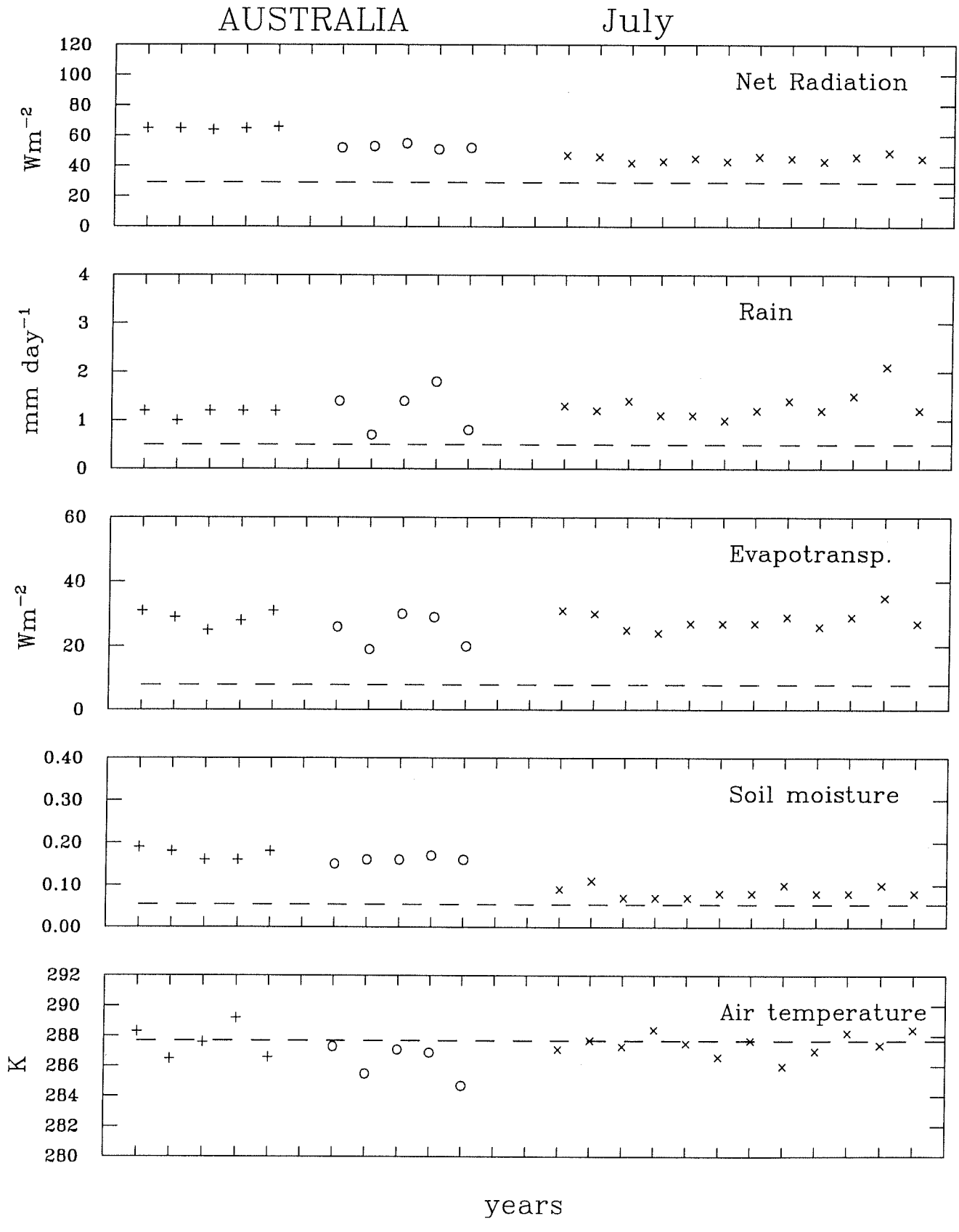

Figure 6: July means of net radiation, precipitation, evapotranspiration, soil moisture and air temperature for simulations: C1 '+', E1 'o' and E2 'x', for Australia.The dashed lines represent observed values.

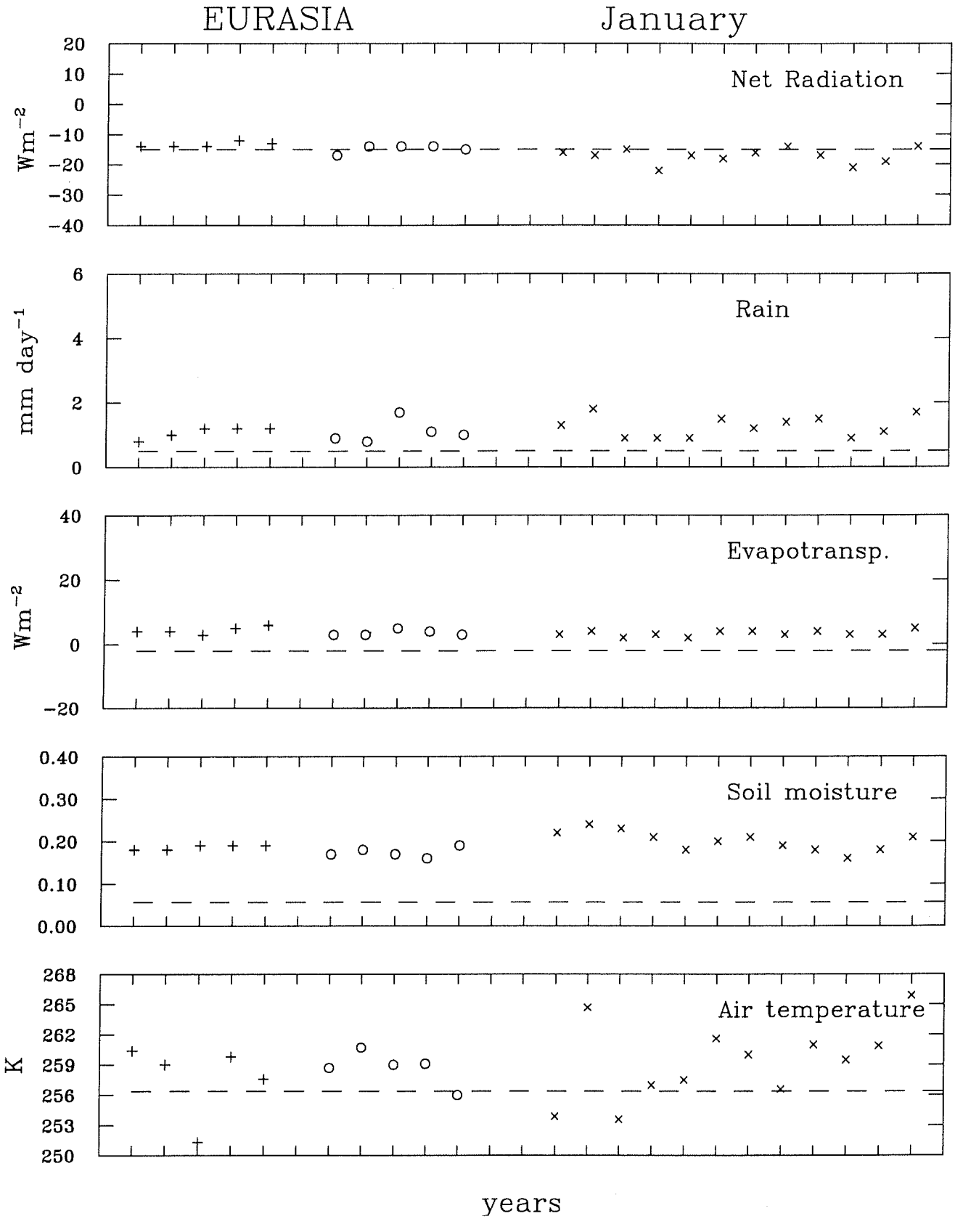

Figure 7: January means of net radiation, precipitation, evapotranspiration, soil moisture and air temperature for simulations: C1 '+', E1 'o' and E2 'x', for Eurasia.The dashed lines represent observed values.

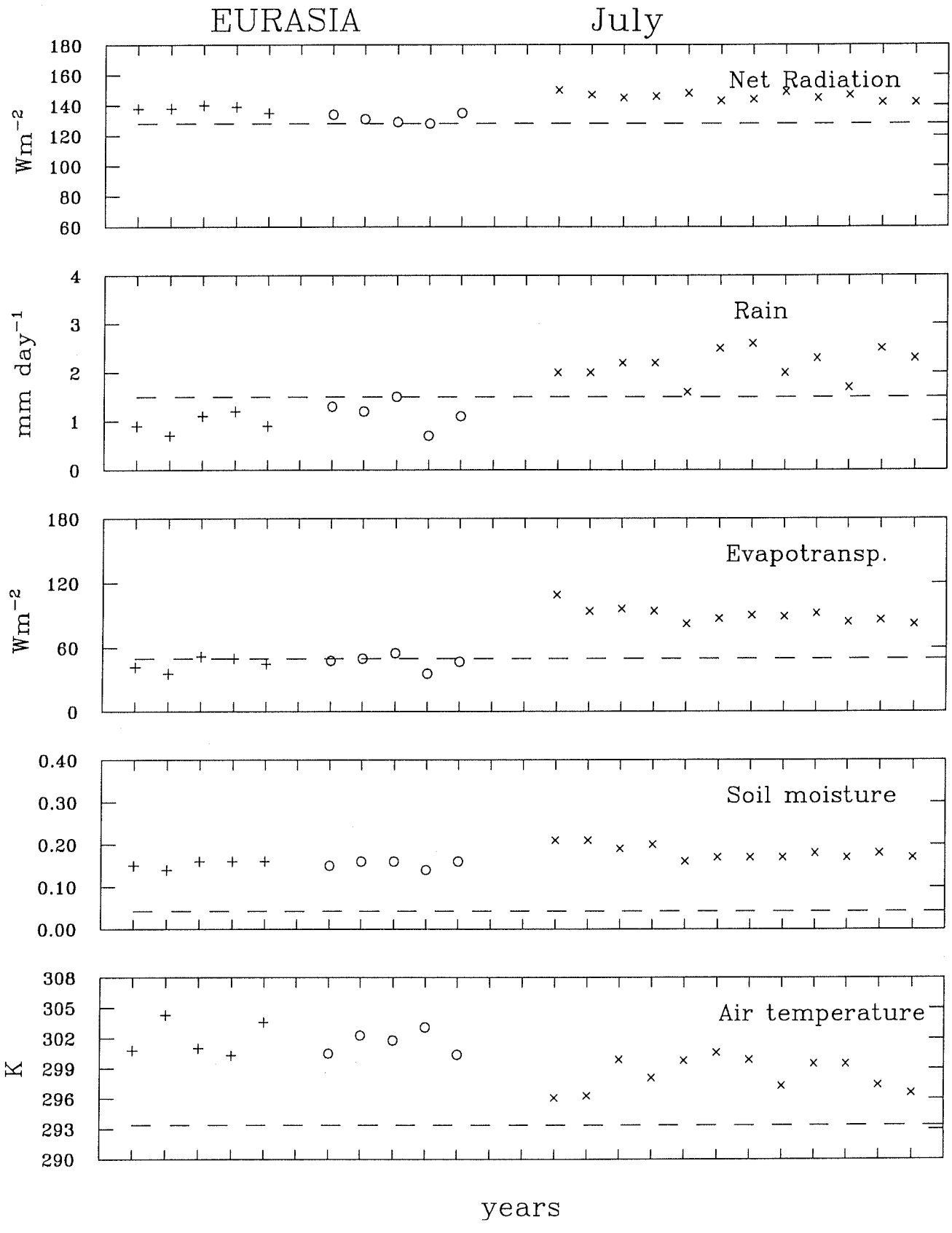

Figure 8: July means of net radiation, precipitation, evapotranspiration, soil moisture and air temperature for simulations: C1 '+', E1 'o' and E2 'x', for Eurasia.

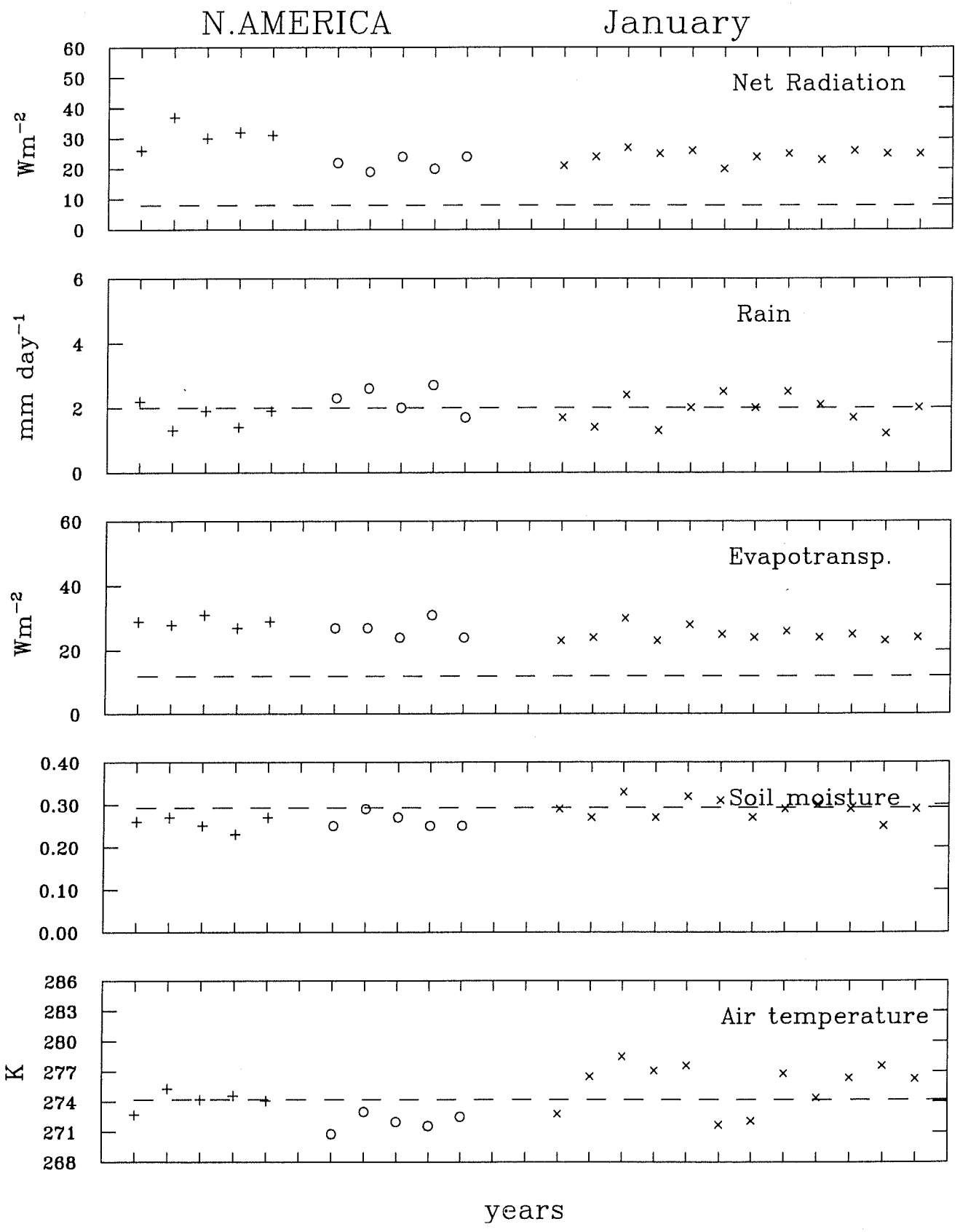

Figure 9: January means of net radiation, precipitation, evapotranspiration, soil moisture and air temperature for simulations: C1 '+', E1 'o' and E2 'x', for North America.The dashed lines represent observed values.

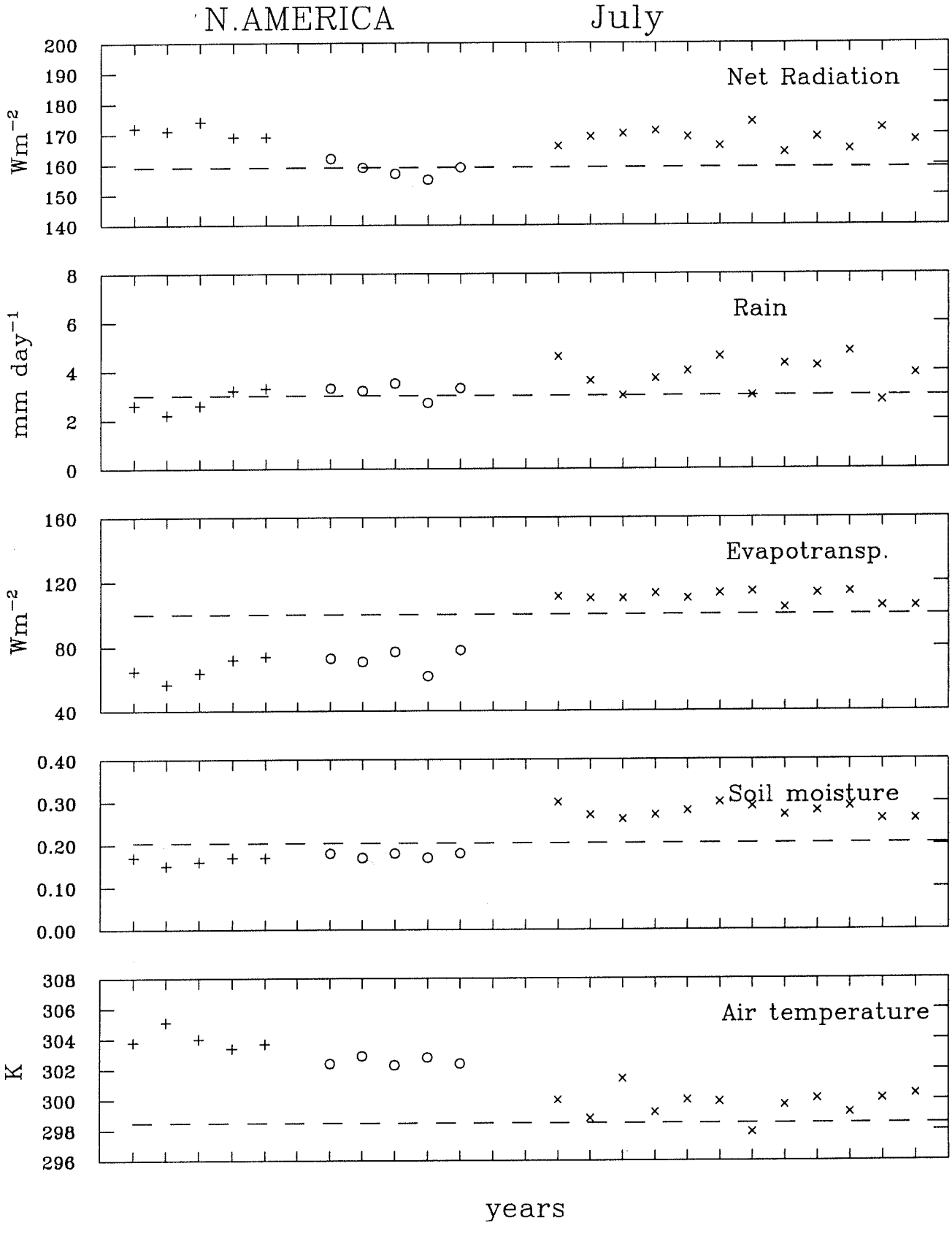

Figure 10: July means of net radiation, precipitation, evapotranspiration, soil moisture and air temperature for simulations: C1 '+', E1 'o' and E2 'x', for North America.

6 Model intercomparison of mean monthly diurnal cycles of surface energy balance components and air temperature for selected regions and stations

Output data for surface fluxes, air and surface temperature and cloud cover were archived at every time step for January and July, for all grid points, for each of the last 5 years of the simulations performed. The data were used to calculate mean monthly diurnal cycles for all grid points. From these we obtained the mean monthly diurnal cycles for some selected stations by interpolation, and in the case of regions by averaging spatially all grid cells within the given area. The effect of the variable time of sunrise and sunset across each region is taken into account during the averaging process. The results for all three simulations described in section 5 are discussed in this section. We focus on regional results, and results for selected stations and comparison with observations.

6a. Single-site observations and comparison with model simulations

We have chosen five sets of observations of mean monthly diurnal cycles of net radiation, and in some cases of sensible and latent heat fluxes and air temperature. The available data are as follows:

1. Amazon region: the mean diurnal cycle of R_N, H, λE and T_a at Manaus, Brazil (2°57′ S, 59°57′ W) for a 30-day period from mid-June to mid-July (e.g. Sato *et al.*, 1989).

2. Australia:

a) the mean diurnal cycle of R_N, H, λE and T_a at Hay, NSW (34°30′ S, 144°56′ E) for a 40-day period through July and August (see Clarke *et al.*, 1971 and Hicks, 1981);

b) the mean diurnal cycle of R_N and T_a at Daly Waters, Northern Territory (16°16′ S, 133°23′ E) for a 30-day period from mid-July to mid-August (see Clarke and Brook, 1979).

3. France: two stations contained within the HAPEX area of south-west France:

a) the mean diurnal cycle of R_N, H, λE and T_a at Caumont (43°41′ N,

0°06′ W), for a 30-day period from mid-June to mid-July, (see e.g. André *et al.*, 1990; data were obtained from the HAPEX group),

b) an analogous data set at Bats (43°38′ N, 0°26′ W).

Comparison of model results with observations must be treated with caution, since the observations represent a single year only. Likely interannual variability must be allowed for; such variability in model mean monthly values is illustrated in Fig. 5 in Garratt *et al.* (1993). The comparison shown here can be indicative only.

For Manaus, there is evidence of a greatly improved simulation of the diurnal cycles with the introduction of the soil/canopy scheme (simulation E2). The partitioning of sensible and latent heat fluxes is particularly realistic, though the air temperatures are now too low as seen in Fig. 11 for the whole Amazonian region. The diurnal cycle of net radiation is improved with the reduced day time maximum related to increased surface albedo and to a sharp increase in the mean cloud cover from 31% in C1 to 38% in E1 and to 59% in E2. Cloud cover is still too low during the night by 20% (hence too low a temperature minimum), and slightly too high (10%) during the afternoon in comparison with observations from the C2 ISCCP Cloud Cover Data. The mean monthly precipitation has increased from about 1.8 in C1 to 3.8 mm day^{-1} in E2, as has the soil moisture content (0.18 to 0.35). This has influenced evaporation, and increased the day time maximum significantly. Accordingly the maximum of the sensible heat flux decreases to close to the observed value. This partitioning of the net radiation is quite realistic. The diurnal cycles of air temperature in C1 and E1 have amplitudes up to 5.6 K higher than observed, with the soil/canopy scheme tending to reduce this, but give temperatures too low by about 2.5 K.

At Hay, no significant improvement is evident, although the reduced diurnal amplitude in air temperature (simulation E2) is closer to the observed value, see Fig. 12.

At Daly Waters, see Fig. 13, the simulated amplitude of the net radiation cycle is significantly lower than the observation, apparently related to simulated cloud cover (0.24) being significantly higher than the observed (0.11).

Comparison of the model results with HAPEX observations at both sites (Samer sites 3 and 7) Caumont and Bats reveals significant improvement when the full soil-canopy scheme is used (simulation E2), with the simulated

diurnal cycles in all variables close to the observed behaviour, see Figs. 14 and 15. The partitioning of energy is quite realistic, and the mean air temperature and diurnal range well represented.

6b. Regional results (January and July)

For each region, January and July results are shown in Fig. 16 to 25, with mean monthly diurnal variations of six variables (R_N, $S_0, R_L, \lambda E$, H, T_a and cloud cover) for the three simulations. Where possible, observed mean monthly values (as shown in earlier Fig.1 to 10) are indicated for reference.

6b1. Africa

In January and July in the African region, (Fig. 16 and 21), the diurnal cycles of net, shortwave radiation and air temperature have similar phases in all simulations, with the highest maxima in the control run (C1) due to lower albedo. The effect of the soil/canopy scheme in E2 is to slightly lower the cloud cover, and to reduce the diurnal amplitude in the air temperature, which in the July case is close to the observed range.

6b2. Amazon Basin

In the Amazon Basin in January (Fig. 17) there is no significant difference between the simulations, being related to high soil moisture content. Day time evaporation rates in C1 and E1 are slightly higher as the evaporation from moist soil is close to the potential, while in E2 the bulk stomatal resistance controls the canopy transpiration. Accordingly the maximum of the diurnal sensible heat cycle is higher in E2. The latent heat profiles tend to oscillate in C1 and E1 indicating some instability in the old surface temperature-evaporation relation. The maximum and minimum temperatures are lower in E2. Cloud cover fractions are similar, with the soil/canopy run having more clouds during the afternoon and less at night.

The July diurnal cycles (Fig.22) of net and shortwave radiation indicate that there is less available energy in E1 and E2 due to higher surface albedo, see Fig. 22. An increase in rain in E2, causes a significant increase in the latent heat flux, and accordingly the sensible heat flux is reduced. Maximum air temperature is lower by up to 4 to 5 K due to higher evaporation. The cloud cover is slightly higher in E2. The July diurnal cycles in E2 are similar to the observations from Manaus.

6b3. Australia

As the canopy is sparse in most of the Australian region there is no evidence of significant impact of the soil/canopy scheme on fluxes and tem-

perature in the E2 simulation. In January, the diurnal cycles of net, and shortwave radiation indicate a lower energy input due to a higher albedo in E1 and E2, see Fig. 18. The July situation is very similar although the magnitudes of the fluxes are different and there is a significant reduction in the amplitude of air temperature, (Fig. 23).

6b4. Eurasia

In the Eurasian region, in January, the major impact of the soil canopy scheme is an increased air temperature, see Fig. 19. This is caused by a much lower mean monthly snow depth, hence a lower surface albedo and increased shortwave flux at the surface. The July profiles in E2 are affected by a two fold increase in precipitation, causing an increase in the evaporation, see Fig. 24. The air temperature profiles are similar at night, but are lower by up to 5 K during the day due to high evaporation, which is closer to the observed range.

6b5. North America

In January, in North America (Fig. 20), the average monthly snow depth has decreased from 7 cm in C1 to 1 cm in E2. This is probably due to decreased cloud cover, hence the incoming shortwave is highest in E2. Also the sensible heat flux and air temperature are highest for this simulation. The July profiles for the soil/canopy simulation are affected by an increase in the evaporation due to a significant increase in the precipitation, (Fig. 25). The maximum air temperature is lower by up to 5 K.

Overall, when the soil/canopy scheme is included, the maximum of the diurnal cycle of evaporation has increased in July for areas with high vegetation cover i.e. Amazon, Eurasia and North America. Also the maximum of the diurnal cycle of air temperature is lower in all the cases except snow covered areas of N.America and Eurasia in January.

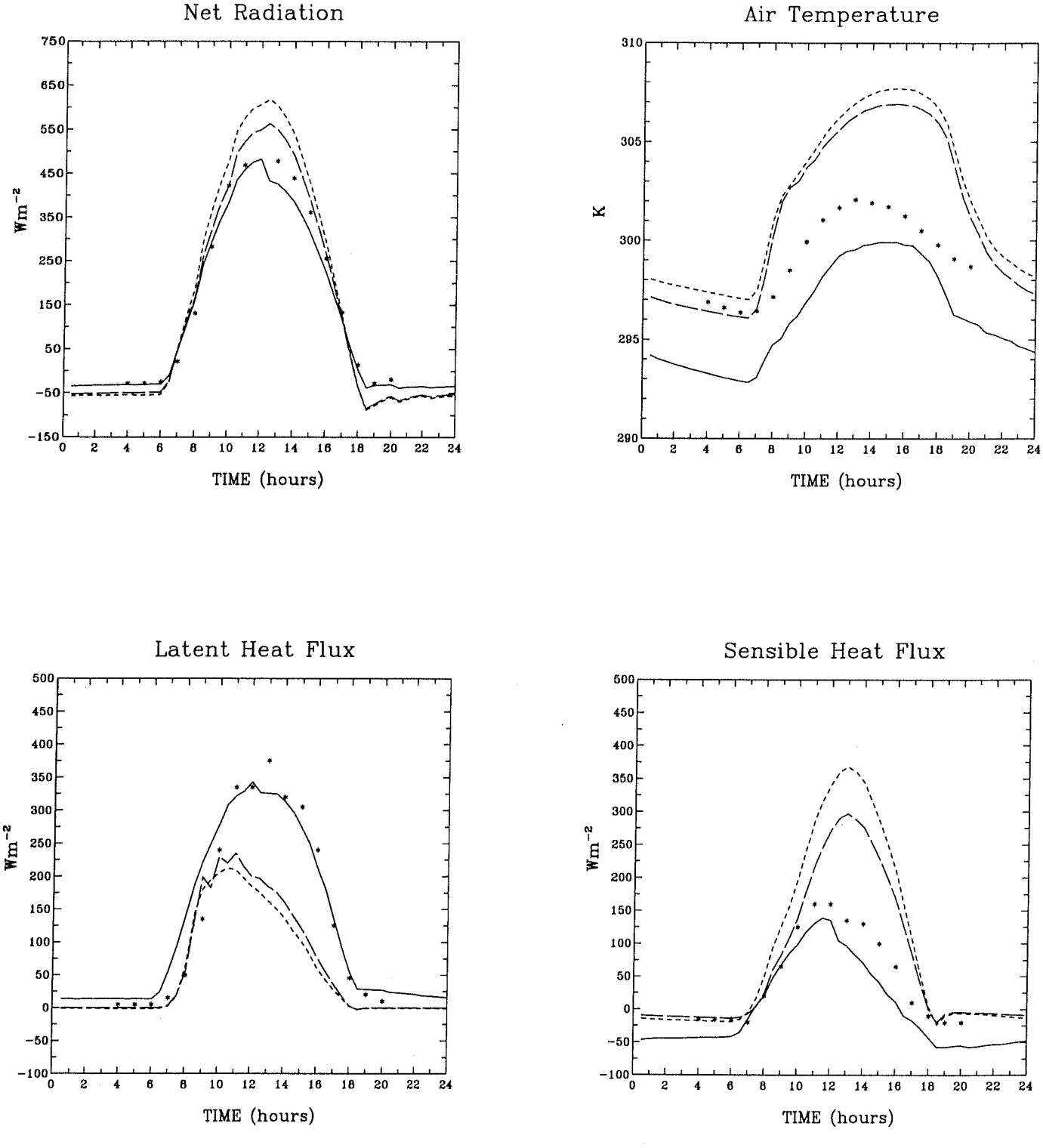

Figure 11: Mean monthly diurnal cycles of net radiation, air temperature, latent and sensible heat fluxes for Manaus, July. Observation - '*', simulation C1 - short pecked curve, E1 - long pecked curve, E2 - continuous curve.

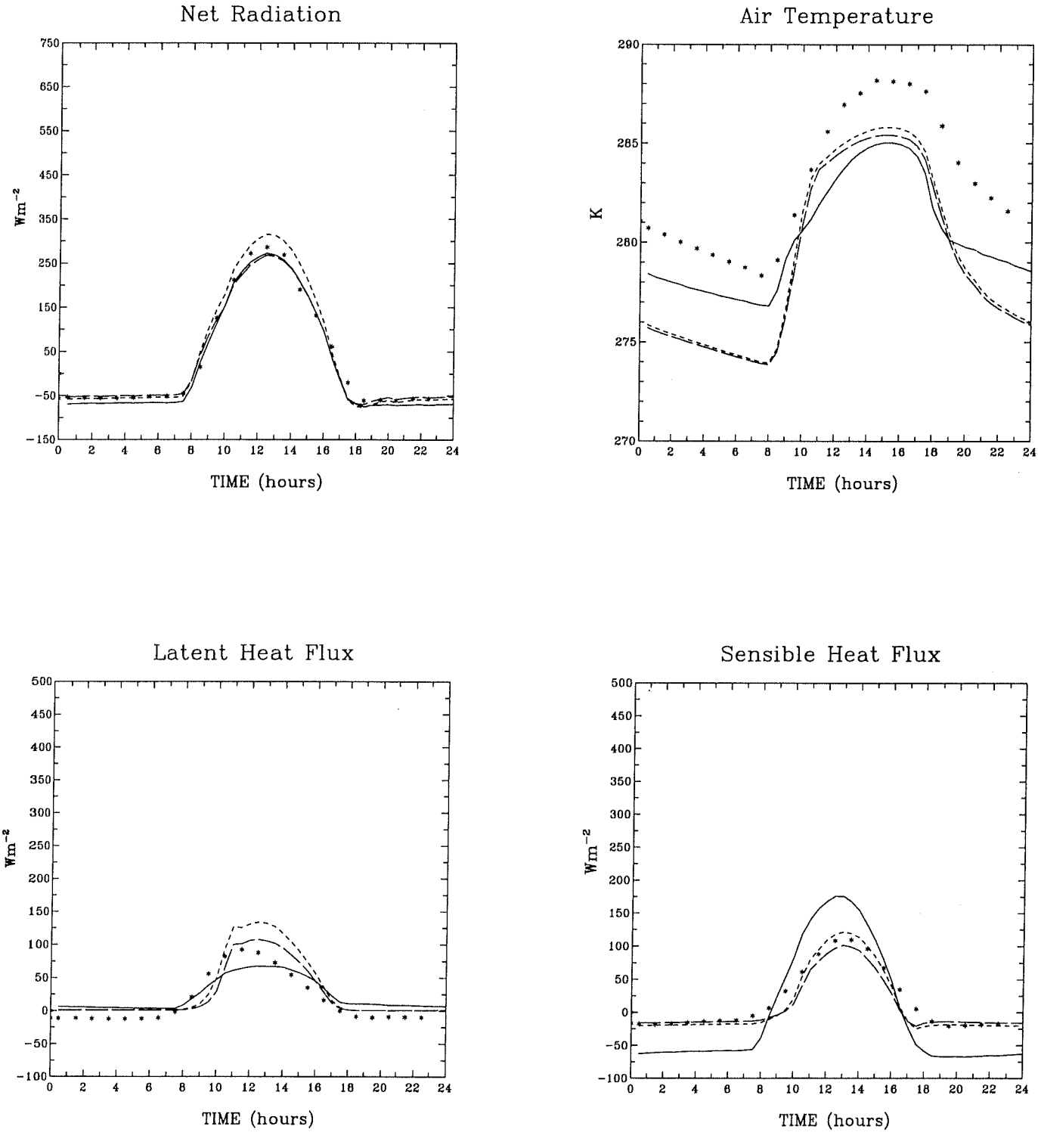

Figure 12: Mean monthly diurnal cycles of net radiation, air temperature, latent and sensible heat fluxes for Hay, July. Observation - '*', simulation C1 - short pecked curve, E1 - long pecked curve, E2 - continuous curve.

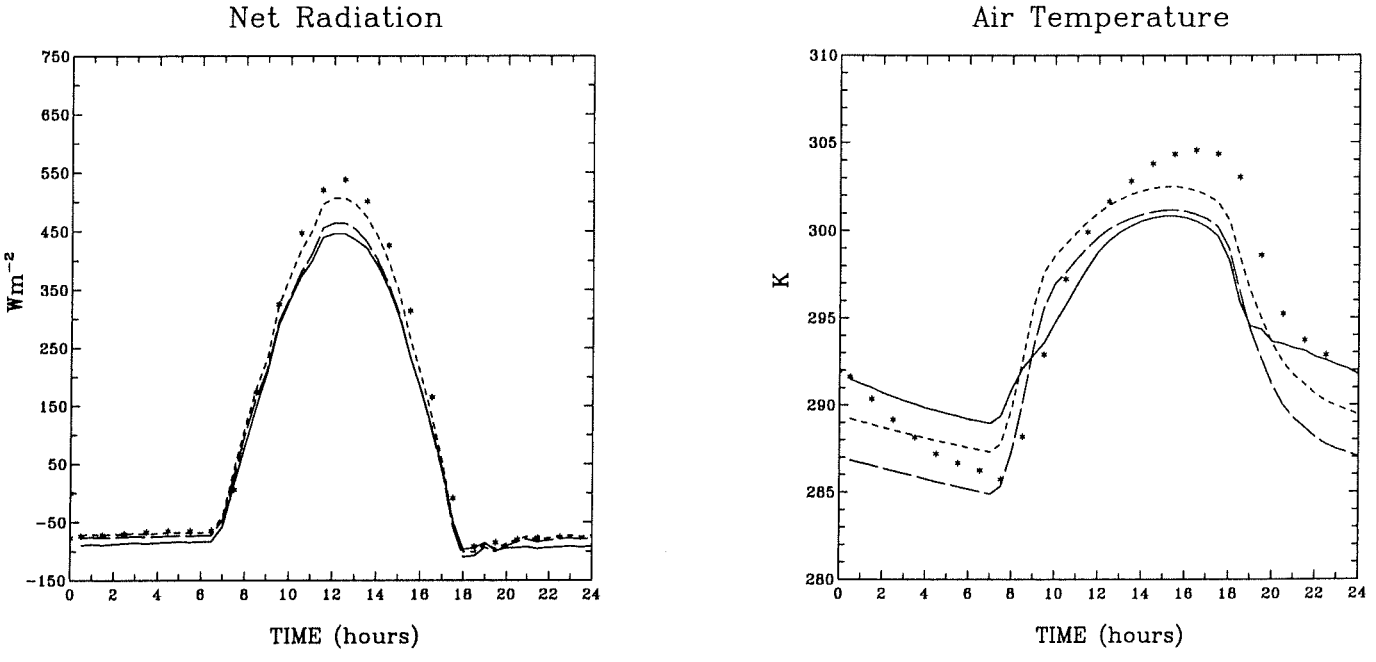

Figure 13: Mean monthly diurnal cycles of net radiation and air temperature for Daly Waters, July. Observation - '*', simulation C1 - short pecked curve, E1 - long pecked curve, E2 - continuous curve.

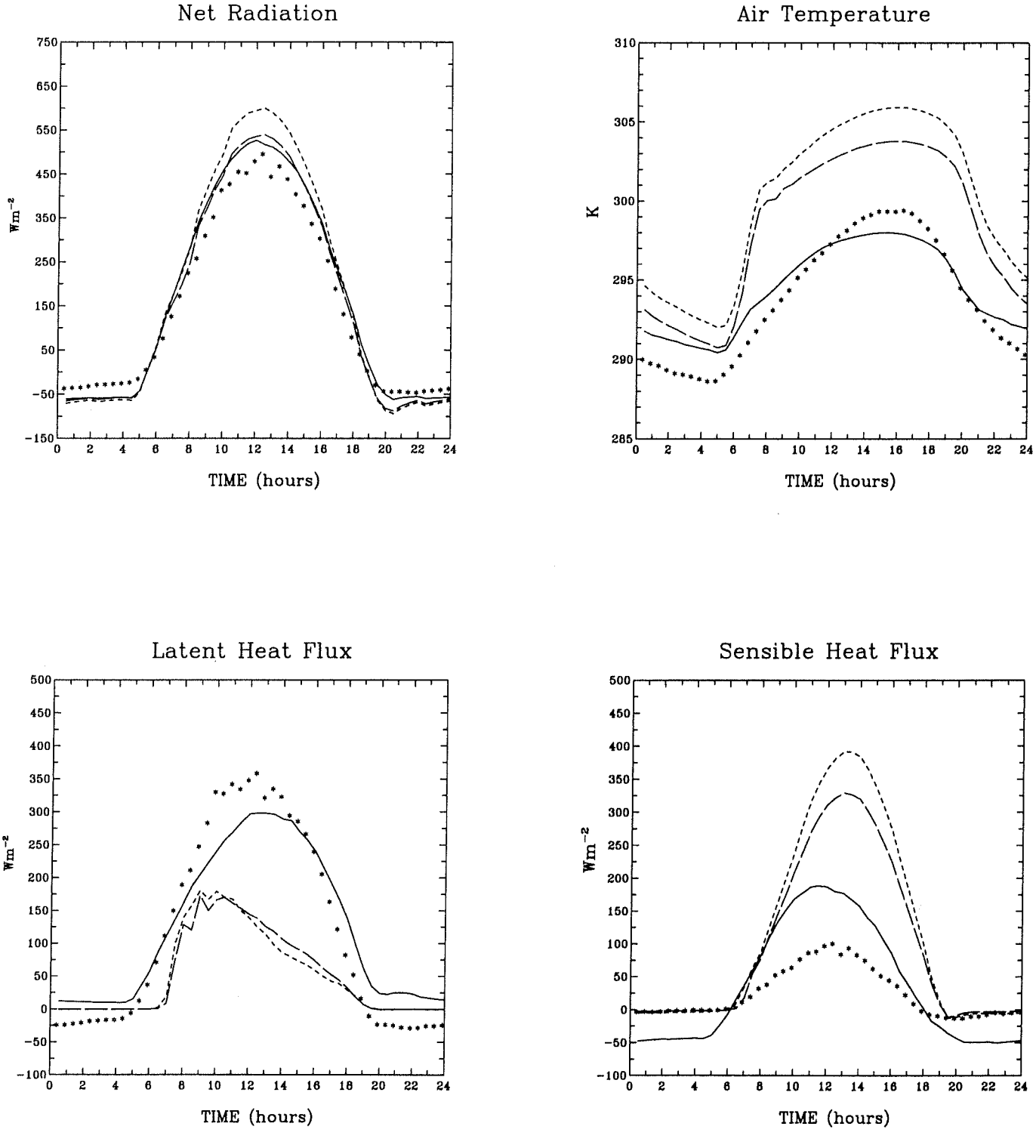

Figure 14: Mean monthly diurnal cycles of net radiation, air temperature, latent and sensible heat fluxes for Caumont (Hapex1), July. Observation - '*', simulation C1 - short pecked curve, E1 - long pecked curve, E2 - continuous curve.

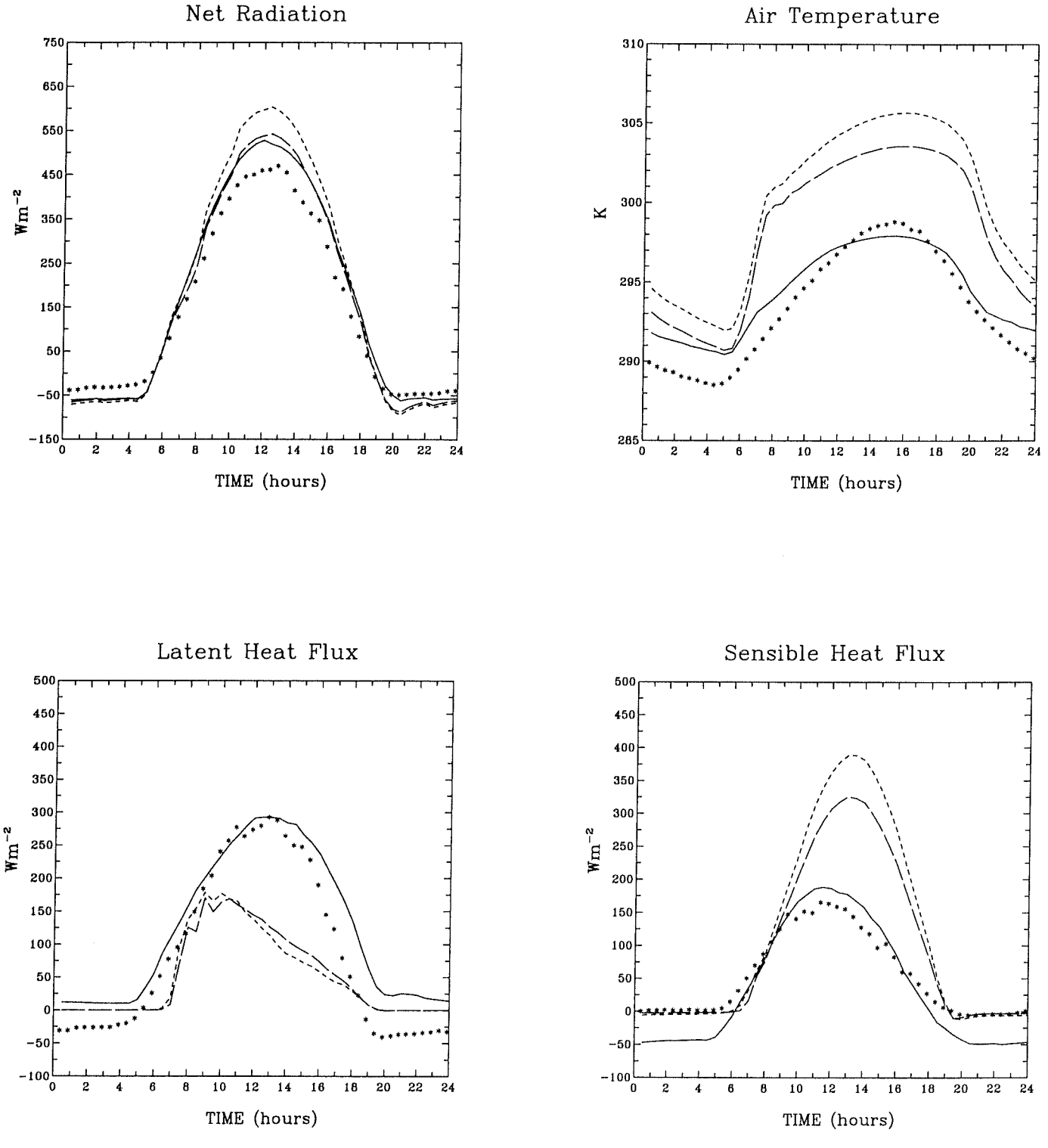

Figure 15: Mean monthly diurnal cycles of net radiation, air temperature, latent and sensible heat fluxes for Bats (Hapex2), July. Observation - '*', simulation C1 - short pecked curve, E1 - long pecked curve, E2 - continuous curve.

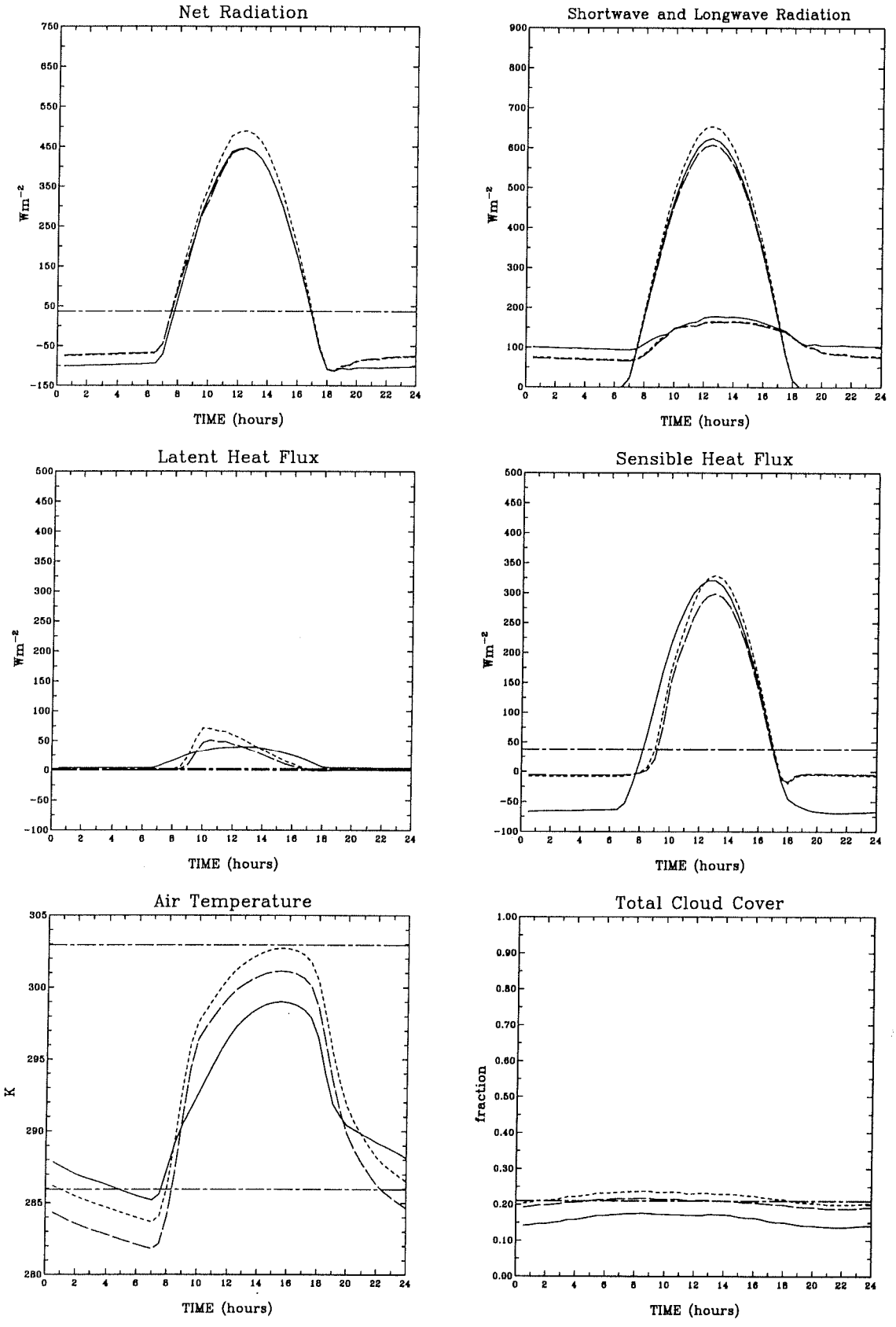

Figure 16: Mean monthly diurnal cycles of net radiation, shortwave and longwave radiation, latent and sensible heat fluxes, air temperature and total cloud cover for Africa, January. Simulation C1 - short pecked curve, E1 - long pecked curve, E2 - continuous curve. Dot-dashed curve represents observed values.

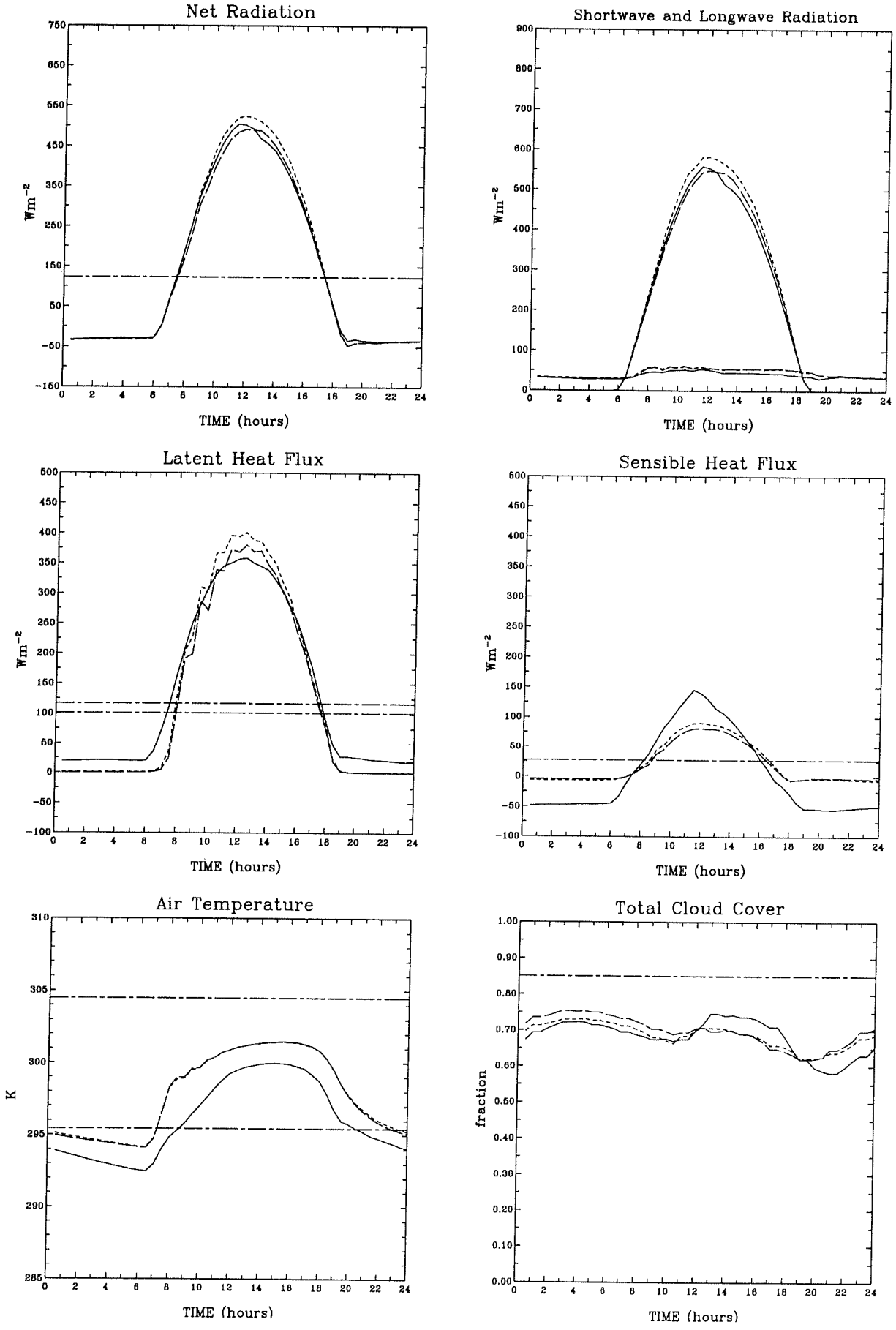

Figure 17: Mean monthly diurnal cycles of net radiation, shortwave and longwave radiation, latent and sensible heat fluxes, air temperature and total cloud cover for Amazon, January. Simulation C1 - short pecked curve, E1 - long pecked curve, E2 - continuous curve. Dot-dashed curve represents observed values.

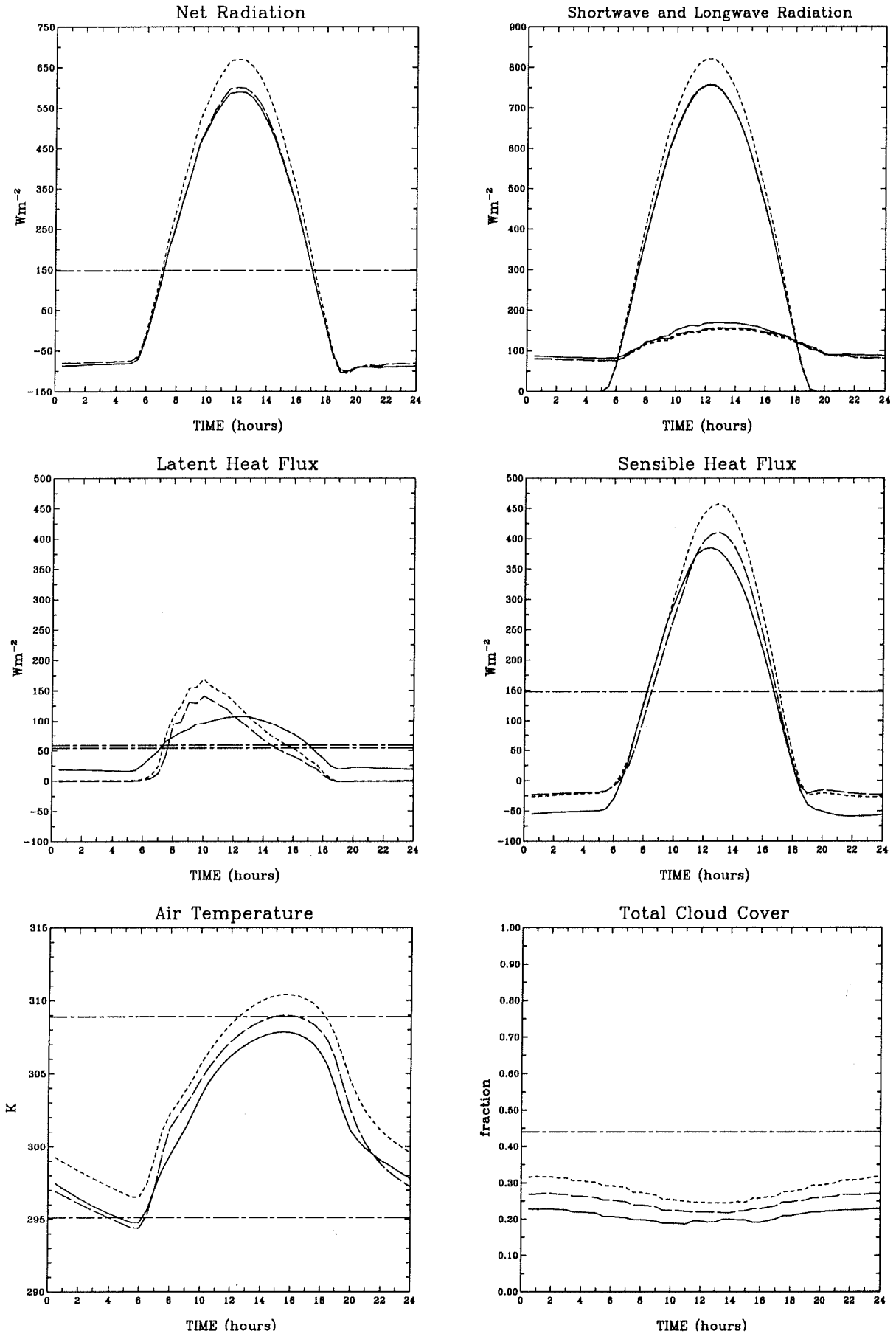

Figure 18: Mean monthly diurnal cycles of net radiation, shortwave and longwave radiation, latent and sensible heat fluxes, air temperature and total cloud cover for Australia, January. Simulation C1 - short pecked curve, E1 - long pecked curve, E2 - continuous curve. Dot-dashed curve represents observed values.

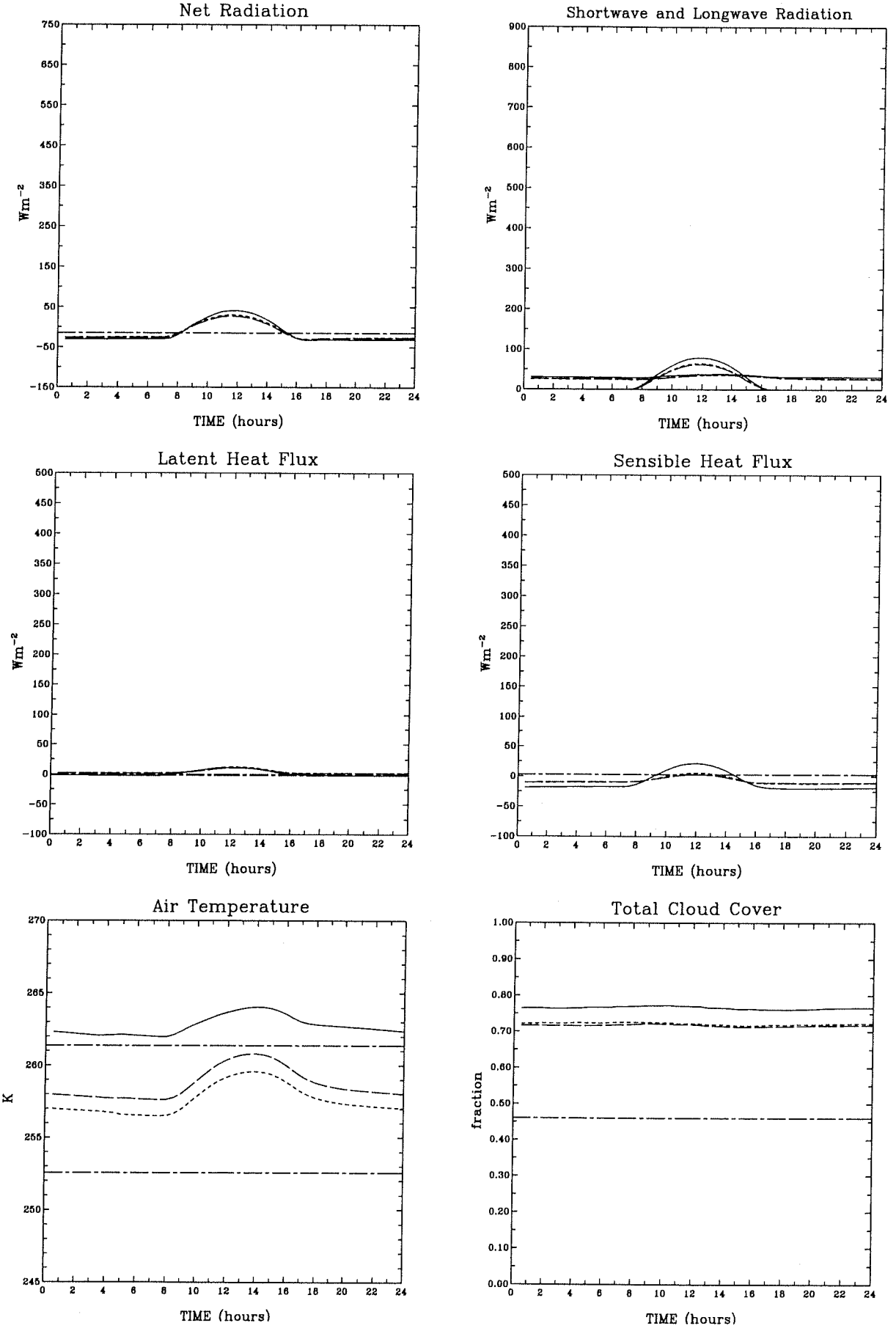

Figure 19: Mean monthly diurnal cycles of net radiation, shortwave and longwave radiation, latent and sensible heat fluxes, air temperature and total cloud cover for Eurasia, January. Simulation C1 - short pecked curve, E1 - long pecked curve, E2 - continuous curve. Dot-dashed curve represents observed values.

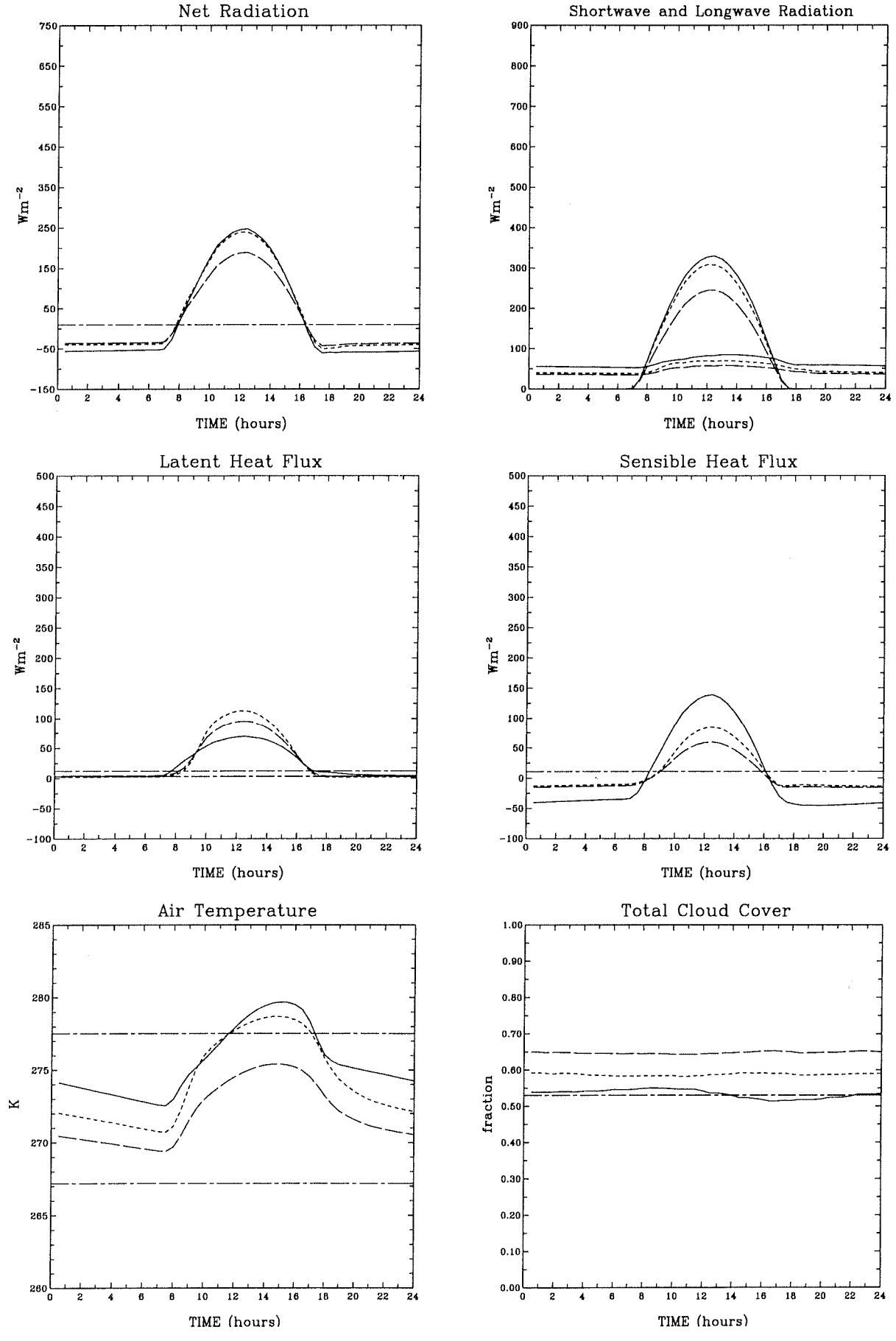

Figure 20: Mean monthly diurnal cycles of net radiation, shortwave and longwave radiation, latent and sensible heat fluxes, air temperature and total cloud cover for North America, January. Simulation C1 - short pecked curve, E1 - long pecked curve, E2 - continuous curve. Dot-dashed curve represents observed values.

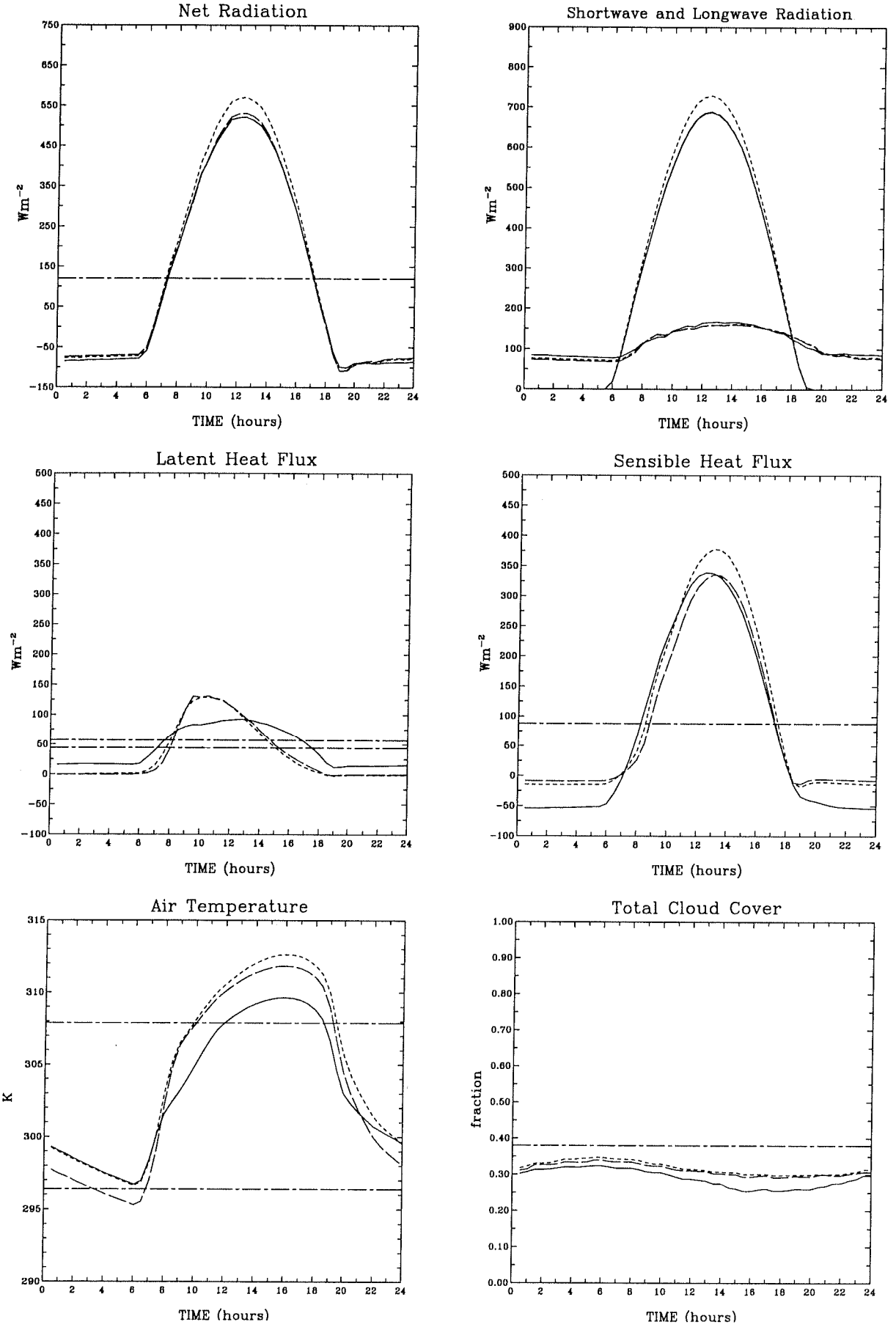

Figure 21: Mean monthly diurnal cycles of net radiation, shortwave and longwave radiation, latent and sensible heat fluxes, air temperature and total cloud cover for Africa, July. Simulation C1 - short pecked curve, E1 - long pecked curve, E2 - continuous curve. Dot-dashed curve represents observed values.

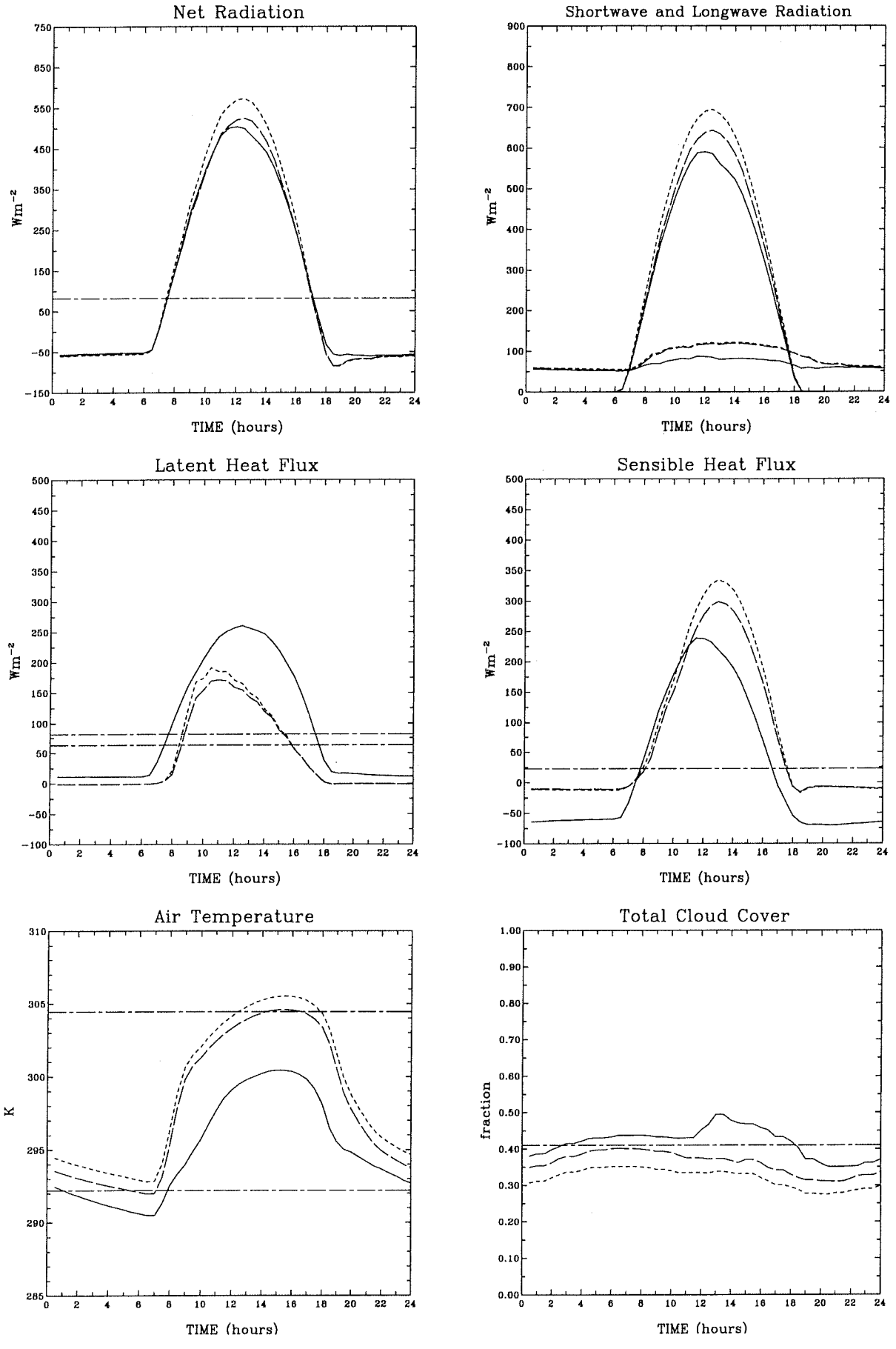

Figure 22: Mean monthly diurnal cycles of net radiation, shortwave and longwave radiation, latent and sensible heat fluxes, air temperature and total cloud cover for Amazon, July. Simulation C1 - short pecked curve, E1 - long pecked curve, E2 - continuous curve. Dot-dashed curve represents observed values.

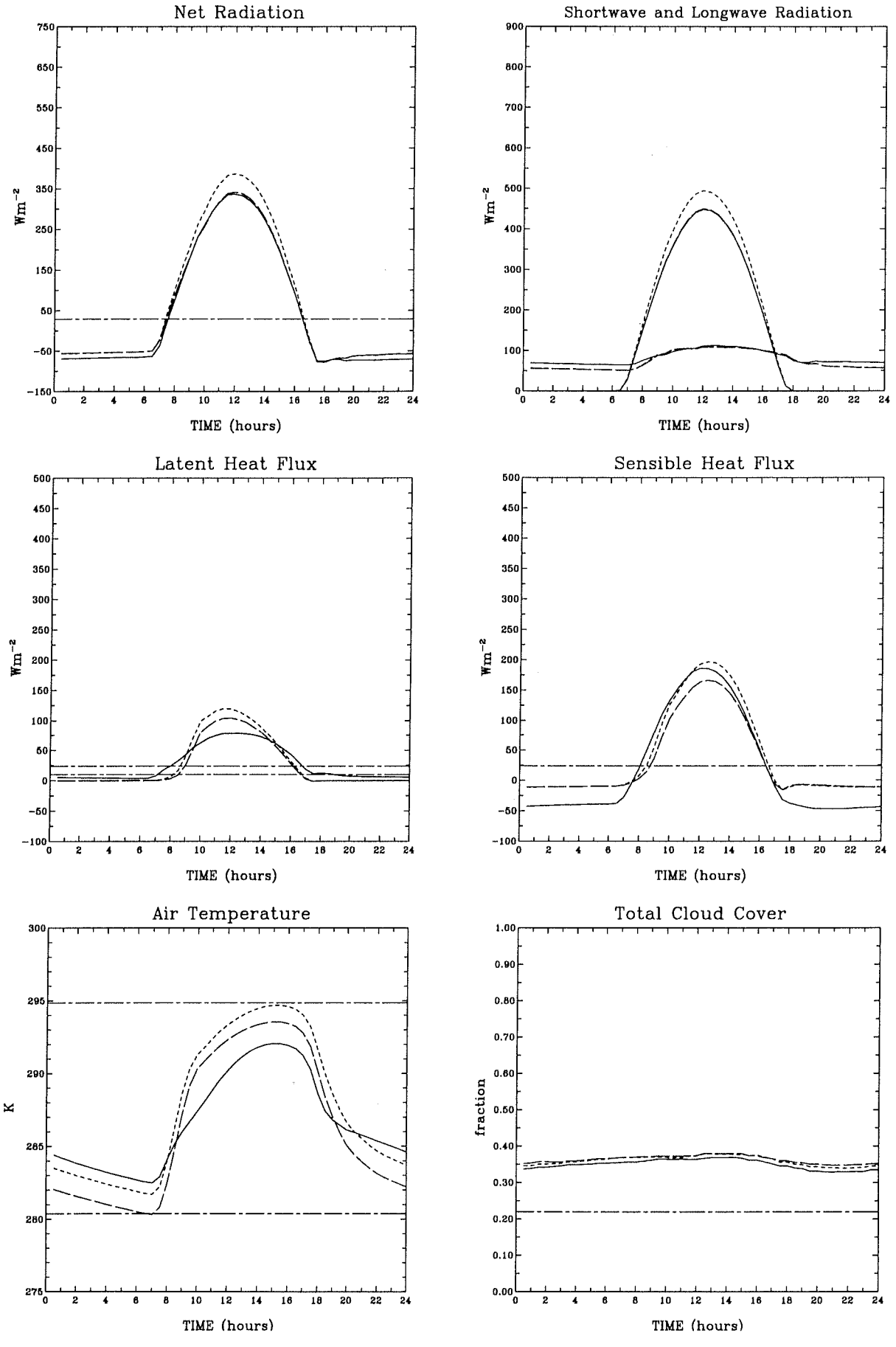

Figure 23: Mean monthly diurnal cycles of net radiation, shortwave and longwave radiation, latent and sensible heat fluxes, air temperature and total cloud cover for Australia, July. Simulation C1 - short pecked curve, E1 - long pecked curve, E2 - continuous curve. Dot-dashed curve represents observed values.

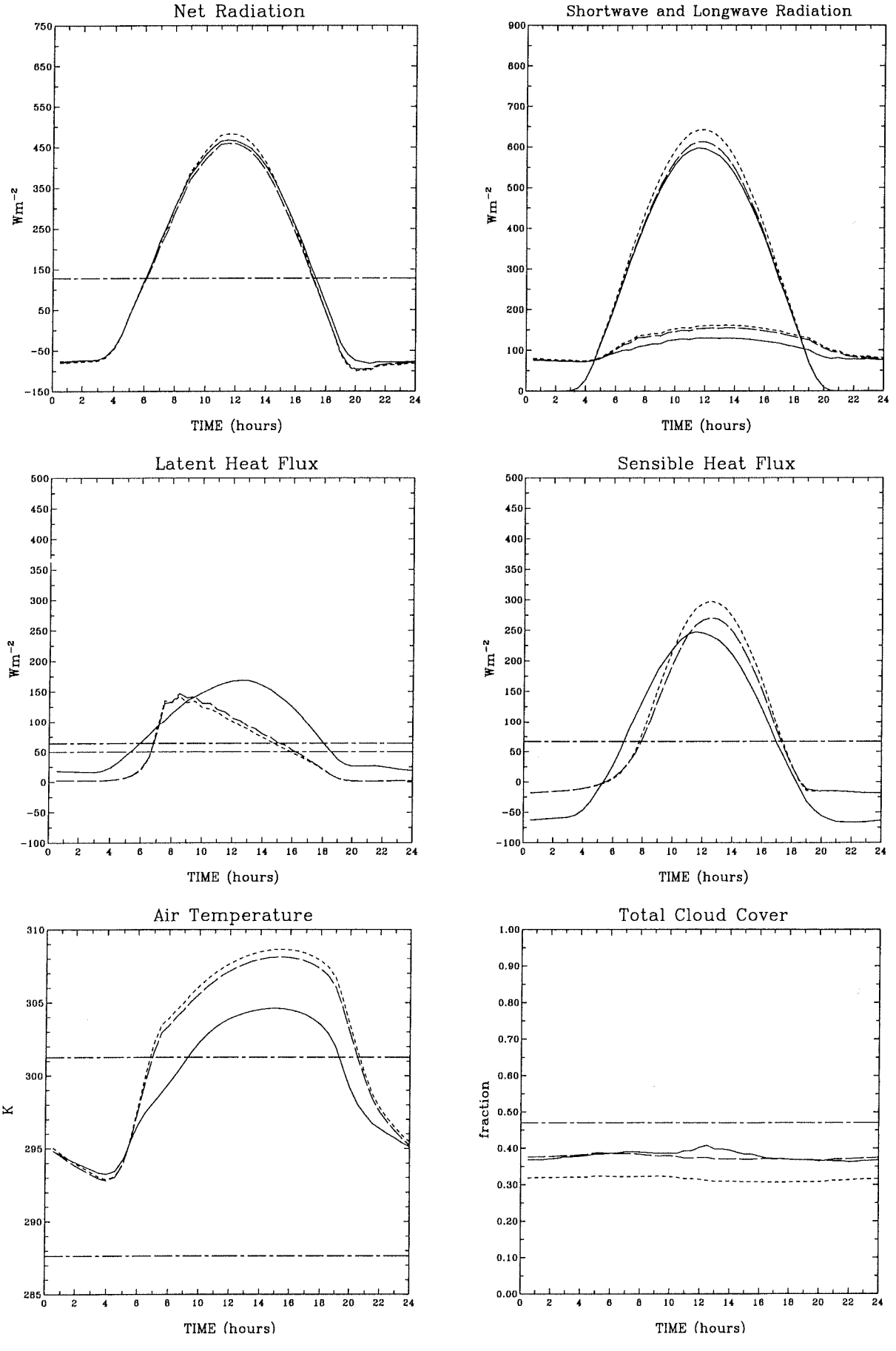

Figure 24: Mean monthly diurnal cycles of net radiation, shortwave and longwave radiation, latent and sensible heat fluxes, air temperature and total cloud cover for Eurasia, July. Simulation C1 - short pecked curve, E1 - long pecked curve, E2 - continuous curve. Dot-dashed curve represents observed values.

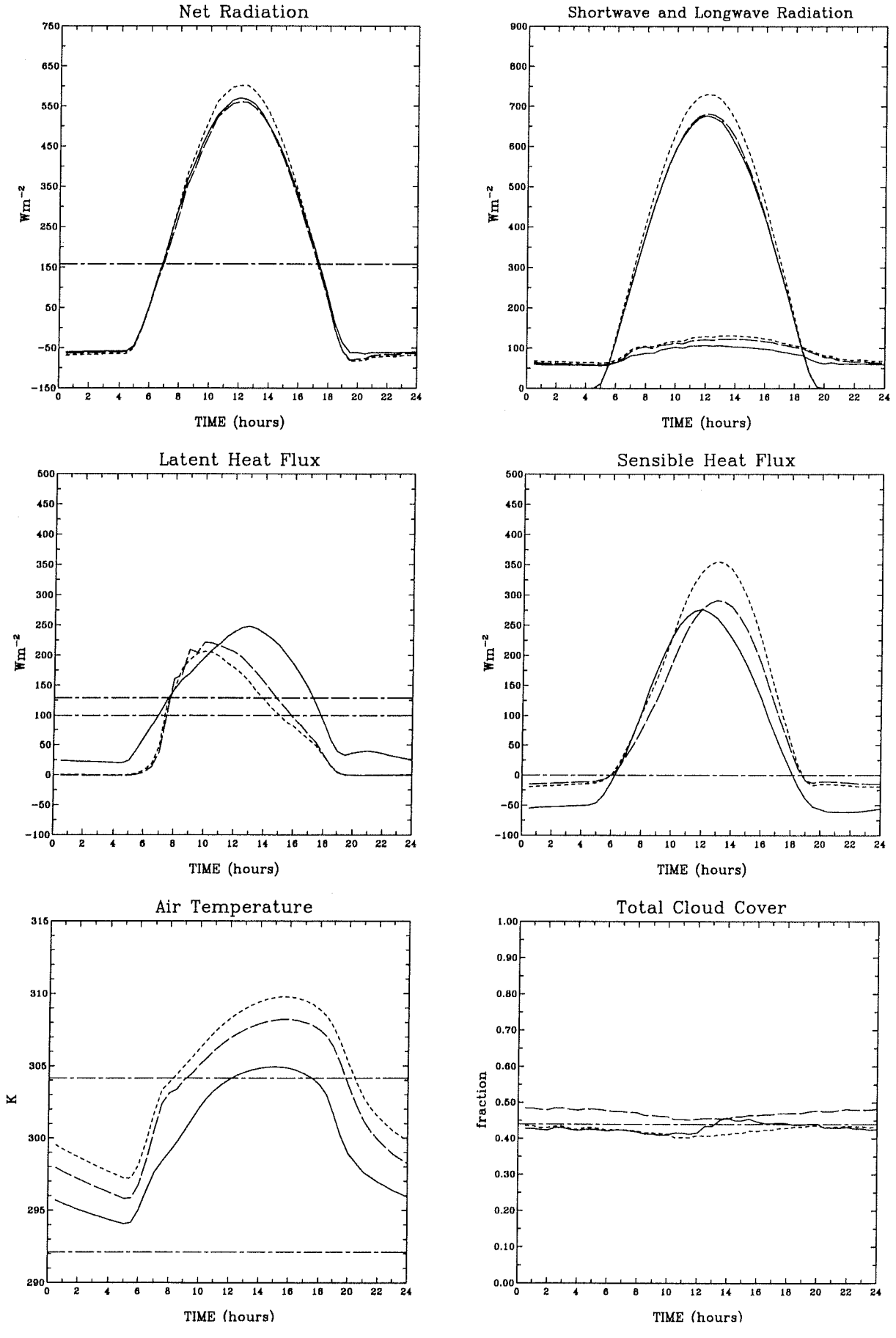

Figure 25: Mean monthly diurnal cycles of net radiation, shortwave and longwave radiation, latent and sensible heat fluxes, air temperature and total cloud cover for North America, July. Simulation C1 - short pecked curve, E1 - long pecked curve, E2 - continuous curve. Dot-dashed curve represents observed values.

7 Model intercomparison of 0D integrations

We have developed a so-called 'zero-dimensional' (0D) version of the scheme to allow testing in a mode decoupled from the GCM. The 0D model is driven by prescribed atmospheric variables, including downward shortwave and longwave radiation, precipitation, air temperature, pressure, humidity and wind speed. The forcing data are obtained by observation or GCM simulation. The 0D model requires at least two years integration before it reaches an equilibrium with the prescribed atmospheric forcing.

To illustrate the differences in model response related to the presence of vegetation, we summarise here the results of integrations with 100% vegetation cover and with bare ground only. Atmospheric forcing data were obtained from a GCM simulation for location (52° N, 0° W), a grassland type surface. Vegetation is characterized by:

- unconstrained stomatal resistance providing physiological control upon evapotranspiration,
- vegetation height, and a surface roughness which can be incorporated into an aerodynamic resistance,
- capacity for interception of rain and dew, thus affecting evaporation and soil moisture,
- vegetation albedo, thus affecting the amount of absorbed shortwave radiation.

For illustrative purposes, and for intercomparison of the simulated surface fluxes and surface temperature, the vegetation and soil albedos were set to the same value. The impact of the canopy under different soil moisture regimes is considered, i.e. 'wet soil' and 'dry soil'.

7a. 'Wet soil' Simulations

In 'wet soil' simulations, soil moisture reservoir is initialised to its full capacity. The mean monthly bulk soil moisture in the bare ground simulation (B1) is lower than in the simulation with vegetation (V1), through the whole year, see Fig. 26a. This is due to an additional resistance exerted by the canopy on transpiration. In the case of evaporation from bare wet soil, this occurs at the potential rate while evapotranspiration is restricted by

the stomata whose resistance is dependent on a number of atmospheric and soil conditions, see Kowalczyk *et al.* (1991). Hence evapotranspiration extracts less water from the wet soil than bare ground evaporation, as shown in the mean monthly evaporation in Fig. 26a. The July mean monthly diurnal cycle of evaporation in B1 has a significantly higher maximum than in V1, see Fig. 27. The higher sensible heat flux in V1 is due to both lower evaporation and lower soil heat flux beneath the vegetation. In simulation B1 a significant part of the net radiation is transformed into soil heat flux. Consequently, the mean monthly diurnal cycle of surface temperature in B1 has a lower maximum. Shortwave radiation and air temperature are prescribed.

7b. 'Dry soil' Simulations

In the case of the 'dry soil' simulations, soil moisture capacity is initialised to half of its full capacity and precipitation is reduced. Similarly, as in the previous experiment, the mean monthly bulk soil moisture in the simulation with bare ground (B2) is lower than in the simulation with vegetation (V2), as seen in Fig. 26b. By July, soil moisture in B2 is depleted below its wilting value, thus restricting evaporation, while evapotranspiration in V2 is still significant as the soil moisture is higher, see Fig. 28. The seasonal cycle of evaporation shows a significantly altered pattern; very high springtime evaporation and lower summer evaporation in B2, (Fig.26b).

On the whole, in both 'wet' and 'dry' experiments under prescribed atmospheric forcing, there is a significant decrease in soil moisture when vegetation is removed.

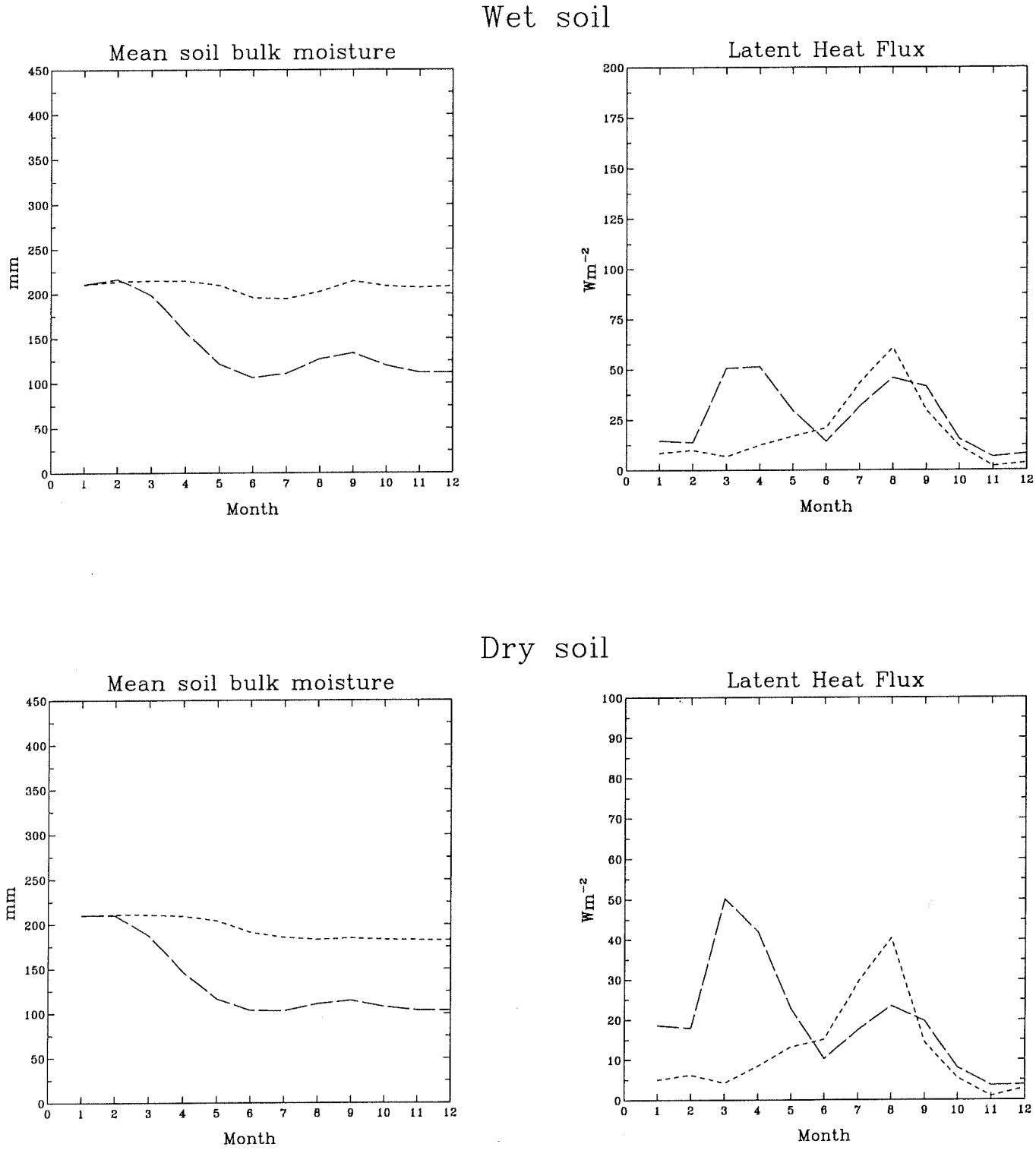

Figure 26: Mean monthly soil bulk moisture and latent heat flux; a) under wet soil condition, b) under dry soil condition. Simulation V1 (vegetation) - short pecked curve, B1 (bare soil) - long pecked curve.

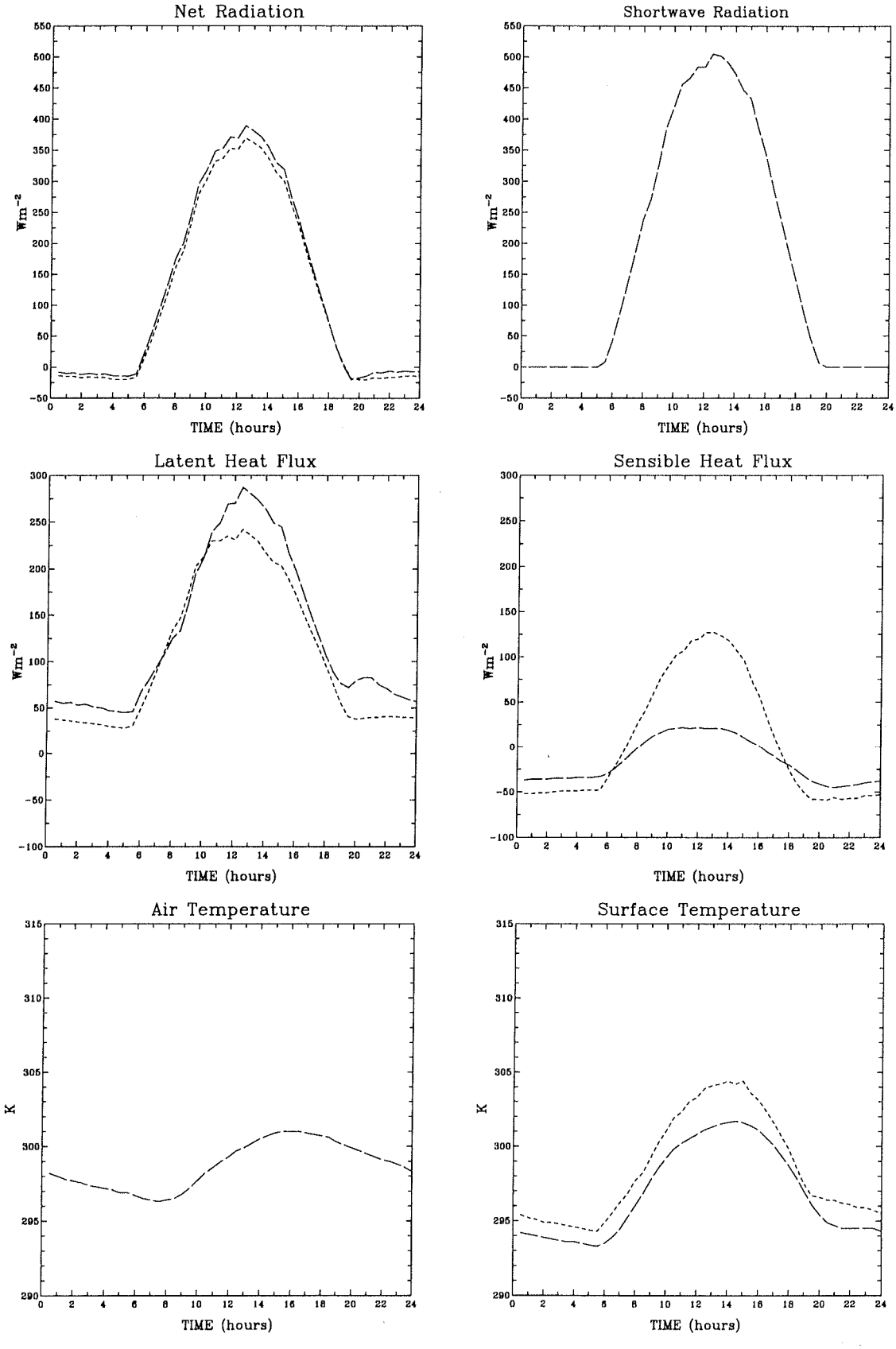

Figure 27: Mean July diurnal cycles of net radiation, shortwave radiation, latent and sensible heat fluxes, air and surface temperature, under wet soil condition. Simulation V1 (vegetation) - short pecked curve, B1 (bare soil) - long pecked curve.

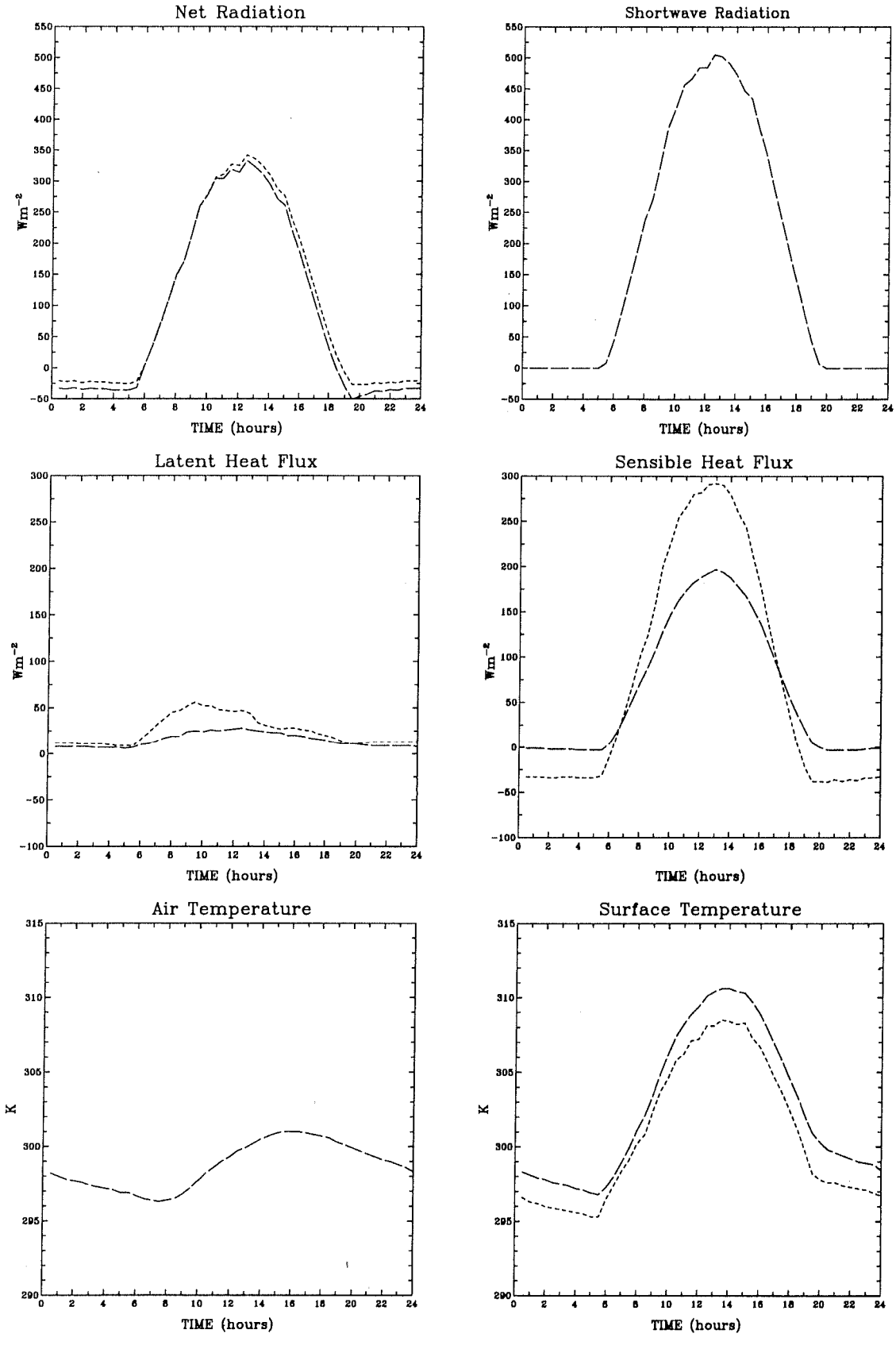

Figure 28: Mean July diurnal cycles of net radiation, shortwave radiation, latent and sensible heat fluxes, air and surface temperature, under dry soil condition. Simulation V1 (vegetation) - short pecked curve, B1 (bare soil) - long pecked curve.

8 Sensitivity of the global and continental scale water balance to changes in subgrid scale precipitation distribution

The global hydrological cycle is an important component of general circulation climate modelling. From the mass conservation principle, it can be assumed that for the whole globe the mean yearly total evaporation is equal to the mean yearly precipitation. Over the oceans, evaporation is greater than precipitation. This difference is offset by the runoff from land, where precipitation exceeds evaporation. There are a number of studies which calculate evaporation and precipitation on a global and continental scale. Comparison of model derived values of global and continental water balance components with the existing studies would give a means of assessing different parametrisations involved in the hydrologic cycle, especially its terrestial component.

Here, the main aim is to evaluate the sensitivity of the global and continental scale water balance to changes in representation of sub-grid scale precipitation distribution. The scheme described below should be included in the 9-level GCM in the near future. GCMs generate precipitation as a consequence of two processes i.e. large scale condensation and moist convection. Large scale condensation usually occurs on large spatial scales, related to areas greater than 10^4 to 10^5 km^2, while moist convection is constrained to an area on the order of 10 to 100 km^2 typically. A GCM grid varies between $2° \times 2°$ to $5° \times 5°$ in size, and with a significant amount of spatial averaging simulated precipitation falls uniformly over the grid cell. This generates too infrequent high intensity precipitation events, and consequently the runoff is generally underestimated. The low spatial resolution of GCMs thus requires the hydrological scheme to incorporate the representation of sub-grid scale variability of precipitation.

The Warrilow *et al.* (1986) and Shuttleworth (1988) precipitation distribution scheme is used here - see derivation details in Warrilow *et al.* (1986). The assumption about the statistical distribution of precipitation and soil infiltration at the subgrid scale allows us to derive a simple expression for surface runoff. The runoff from the surface (R_{sf}) in the absence of vegetation, occurs when the net flux of water P_s at the surface exceeds the infiltration rate F_s. R_{sf} is represented by

$$R_{sf} = P_s exp(-\mu F_s / P_s). \qquad (22)$$

In the presence of a canopy, when interception by the canopy (P_c) exceeds the maximum canopy infiltration rate (F_c), canopy drip occurs. R_{drip} is represented by

$$R_{drip} = P_c exp(-\mu F_c / P_c). \tag{23}$$

Decreasing the fraction of the grid cell, μ, receiving convective and large scale precipitation may lead to different hydrological situations, as surface runoff is increased while soil moisture content is decreased. The main problem here is an *a priori* choice of the appropriate value of μ. Ideally this parameter should represent the fraction of the grid occupied by the precipitating clouds; however this is not a diagnostic variable in the CSIRO9 GCM. In most GCMs at present, the parameter μ for large scale condensation (μ_l) is usually taken between 0.6 and 1.0, while for moist convection its value (μ_c) may vary from 0.05 to 0.3. In reality, this parameter will vary in time and space.

8a. '0D' Simulations

Firstly, a sensitivity of the local climate to variations in μ is explored by using the '0D' model with an atmospheric forcing for tropical forest. Table 4 presents a summary of the results for two cases i.e. land dominated by vegetation cover ($\sigma_f = 0.9$, simulations Y1 to Y5) and ground with sparse cover ($\sigma_f = 0.1$, simulations X1 to X5). At each model time step, precipitation is divided into a large scale component, and a moist convection component, taken as 0.7 and 0.3 respectively of the total precipitation. Separate values of μ are assigned to each type of precipitation.

Run	σ_f	μ_l	μ_c	E (mm)	Runoff (mm)
x1	0.1	1.0	1.0	1586	1685
X2	0.1	0.3	0.3	904	2370
X3	0.1	0.1	0.1	359	2911
X4	0.1	1.0	0.3	1508	1764
X5	0.1	1.0	0.1	1452	1820
Y1	0.9	1.0	1.0	1730	1539
Y2	0.9	0.3	0.3	1254	2016
Y3	0.9	0.1	0.1	689	2578
Y4	0.9	1.0	0.3	1666	1604
Y5	0.9	1.0	0.1	1616	1653

Table 4: '0D' model simulations summary.

The total yearly precipitation of 3272 mm is partitioned between evaporation and runoff. The most drastic cut in evaporation occurs when both types of precipitation are falling on a fraction of a grid cell. The cases with only the convective rain area limited, i.e. $\mu_c = 0.3$ and 0.1, have a smaller decrease in the evaporation as moist convection here contains only 0.3 of the total precipitation. In reality, the frequency and intensity of the moist convection events depend on season and geographical position. Also, simulations with $\sigma_f = 0.9$ have a higher evaporation than simulations with $\sigma_f = 0.1$, as a significant percentage of the precipitation is intercepted by the tropical forest and evaporated to the atmosphere before reaching the ground. A high sensitivity of the simulated partitioning between evaporation and runoff to the value of μ indicates the importance of the subgrid scale variability of precipitation.

8b. GCM Simulations

Three CSIRO9 GCM simulations were performed, each of four years' length, to assess the sensitivity of the water balance components on a global and continental scale to the magnitude of μ. The amount of large scale and convective precipitation is calculated in the model at each grid cell, as described by McGregor *et al.* (1993). In the first simulation, $R1$, both large scale and convective rain occur on the whole GCM grid, i.e. $\mu_l = 1.0, \mu_c = 1.0$. In the second simulation, $R2$, large scale rain is spread over the whole grid, $\mu_l = 1.0$, while convective rain is limited to $\mu_c = 0.3$, and in the third simulation, $\mu_l = 1.0$ and $\mu_c = 0.1$. As shown in Table 5, the model is able to simulate the global values of evaporation and precipitation within the estimates of Henning (1989) and Budyko (1978), although rates of evaporation and precipitation over the land are somewhat low. Runoff fraction $((P_l - E_l)/P_l)$ is underestimated in R1 and R2 and overestimated in R3 in comparison with the estimates of 0.38 to 0.43.

			Evaporation (mm)			Precipitation (mm)			
Run	μ_l	μ_c	**Global (Eg)**	**Land (El)**	**Ocean (Eo)**	**Global (Pg)**	**Land (Pl)**	**Ocean (Po)**	**(Pl-El)/Pl**
R1	1.0	1.0	993	411	1295	994	613	1191	0.329
R2	1.0	0.3	992	407	1294	992	620	1185	0.343
R3	1.0	0.1	957	303	1325	957	568	1158	0.466
Estimates from									
Henning(1989)			952	442	1159	952	718	1047	0.384
Budyko(1978)			1130	450	1400	1130	800	1270	0.430

Table 5: Annual total evaporation and precipitation simulated by GCM and estimated by Henning (1989) and Budyko (1978).

A summary of the continental scale water balance components in Table 6 reveals that in the R1 simulation all continents except Asia, Australia and Antarctica have excessive rain and Africa and South America also have excessive evaporation. Reduction of the moist convection spatial scale (μ_c) in R2 reduces evaporation in Africa, South America and North America. Precipitation is slightly reduced in Asia, South America and Europe, and increased in Australia. Also the runoff is increased in all the continents except Antarctica. Simulation R3 brings significant reduction in both precipitation and evaporation in Africa, South America and Australia. The evaporation there is now underestimated and runoff overestimated. Comparison of the three simulations shows that simulation R2 gives the best agreement with Willmott *et al.* (1985) calculations. The runoff has increased in all the continents except Antarctica and is close to estimates of Willmott. Precipitation and evaporation are still too high in Africa and South America, and far too low in Antarctica. Overall it is clear that the regional climate is sensitive to the precipitation distribution on the subgrid scale. The spatial variability of precipitation induces increased surface runoff, thus affecting soil moisture and evaporation.

Region	R1	R2	R3	Henning	Willmott	
	2.2	2.2	1.8	1.9	1.7	Prec (mm/day)
Africa	1.9	1.7	1.0	1.4	1.3	Evap (mm/day)
	0.4	0.6	1.0	0.5	0.4	Runoff (mm/day)
	4.9	4.8	4.5	4.1	4.2	Prec (mm/day)
South America	3.5	3.1	2.3	2.4	2.7	Evap (mm/day)
	1.5	1.7	2.4	1.6	1.5	Runoff (mm/day)
	2.0	2.0	1.9	1.7	1.6	Prec (mm/day)
North America	1.3	1.2	1.1	1.1	1.2	Evap (mm/day)
	0.5	0.6	0.7	0.6	0.4	Runoff (mm/day)
	1.3	1.5	1.2	1.3	1.4	Prec (mm/day)
Australia	1.5	1.5	1.0	1.1	1.5	Evap (mm/day)
	0.0	0.2	0.5	0.1		Runoff (mm/day)
	2.1	2.0	2.0	1.9	2.3	Prec (mm/day)
Asia	1.2	1.2	1.1	1.1	1.5	Evap (mm/day)
	0.6	0.8	0.9	0.8	0.8	Runoff (mm/day)
	1.9	1.7	1.7	1.6	1.6	Prec (mm/day)
Europe	1.1	1.1	1.0	1.0	1.2	Evap (mm/day)
	0.4	0.5	0.6	0.6	0.3	Runoff (mm/day)
	0.1	0.1	0.1	0.6		Prec (mm/day)
Antarctica	0.0	0.0	0.0	0.0		Evap (mm/day)
	0.0	0.0	0.0	0.6		Runoff (mm/day)

Table 6: Continental water balance components simulated by GCM and estimated by Henning (1989) and Willmott *et al.* (1985).

Final Comments

We have assessed the impact of a new soil-canopy scheme on aspects of the regional surface energy and water balances as simulated in the CSIRO 9-level GCM. Attention has been given to mean monthly statistics, both in the form of overall averages and the mean diurnal variation of a range of properties. Overall, we believe significant improvements have resulted from this modification to the surface representation in the model. The performance of our surface scheme in relation to a range of schemes being used around the world is being tested in an intercomparison study known as 'Project for Intercomparison of Land-surface Parameterization Schemes' (PILPS), Henderson-Sellers *et al.* (1993). Detailed results are not available at the time of publication of this Technical paper.

We have only dealt with the impact of the new scheme on simulations of surface-related climate in the 9-level GCM. We also did analogous analyses with the 4-level GCM; results from these latter simulations have been analysed in the context of global tropospheric statistics (Ian Watterson, priv. comm.). He concluded as follows: 'Remote effects on tropospheric winds and surface pressures were fairly small but, on the whole, were probably an improvement. The cold bias in the troposphere remained'. The new scheme and improved land surface albedos 'have the potential to reduce the northern summer biases in the model.'

As a final comment, we should point out that the surface scheme has now been successfully implemented in the limited area model (LAM) and Lagrangian atmospheric dispersion model (LADM). Of course, there are weaknesses in our new scheme as with most schemes. Aspects of the snow accumulation and melt formulations need attention, surface albedos can be upgraded in the near future and subgrid hydrological processes should be included as time allows.

References

Albrecht, F. 1961: Der jährliche Gang der Komponenten des Wärme- und Wasserhaushaltes der Ozeane. – Berichte des Deutschen Wetterdienstes, **11** (79): 24 pp. Offenbach a.M.

André, J.C., Bougeault, P., Goutorbe, J.P., 1990: Regional Estimates of Heat and Evaporation Fluxes over Non-homogenous Terrain. Examples from the Hapex-Mobilhy Programme. *Bound. Layer Meteor.*, **50**, 77-108.

Budyko, M.I., 1978: *The Heat Balance of the Earth*, in: Gribbin, J. (ed.), Climate Change, pp. 85-113., Cambridge University Press.

Clarke, R. H., and R. R. Brook, 1979: The Koorin Expedition - Atmospheric Boundary Layer Data over Tropical Savannah Land. Dept. of Science, Canberra, 359 pp.

Clarke, R.H., Dyer, A.J., Brook, R.R., Reid, D.G. and A.J. Troup, 1971: The Wangara Experiment: Boundary-Layer Data. Tech. Paper No.19, Div. Meteor. Physics, CSIRO, Australia. 21 pp.

Deardorff, J.W., 1978: Efficient Prediction of Ground Surface Temperature and Moisture, with Inclusion of a Layer of Vegetation. *J. Geophys. Res.*, **83**, 1889-1903.

Dickinson, R.E., 1984: Modeling Evapotranspiration for Three Dimensional Global Climate Models. Climate Processes and Climate Sensitivity. *Geophys. Monogr.*, **29**, 58-72.

Dorman, J.L. and P.J. Sellers, 1989: A Global Climatology of Albedo, Roughness Length and Stomatal Resistance for Atmospheric General Circulation Models as Represented by the Simple Biosphere Model (SiB). *J. Appl. Meteor.*, **28**, 833-855.

Dutton, E.G., 1990: Annual Forcing of the Surface Radiation Balance Diurnal Cycle Measured from a High Tower near Boulder, Colorado. *J. Climate*, **3**, 1400-1408.

Garratt, J.R., 1992: *The Atmospheric Boundary Layer.* Cambridge University Press, 316 pp.

Garratt, J.R., 1993: Sensitivity of Climate Simulations to Land-Surface and Atmospheric Boundary-Layer Treatments - A Review, *J. Climate*, **6**, 419-449.

Garratt, J.R., 1994: Incoming Shortwave Fluxes at the Surface - A Comparison of GCM Results with Observations. *J. Climate*, **7**, 72-80.

Garratt, J.R., Krummel, P.B., Kowalczyk, E.A., 1993: The Surface Energy Balance at Local and Regional Scales - A Comparison of General Circulation Model Results with Observations, *J. Climate*, **6**, 1090-1109.

Gates, D.M., 1980: *Biophysical Ecology.* Springer-Verlag, New York, 611 pp.

Gordon, H.B., 1981: A Flux Formulation of the Spectral Atmospheric Equations Suitable for Use in Long-term Climate Modeling. *Mon. Wea. Rev.*, **109**, 56-64.

Henderson-Sellers, A., Z.-L. Yang and R. E. Dickinson, 1993: The Project for Intercomparison of Land-surface Parameterization Schemes. *Bull. Amer. Meteor. Soc.*, **74**, 1335-1349.

Henning, D., 1989: *Atlas of the Surface Heat Balance of the Continents.* Gebruder Borntraeger, 402 pp.

Hicks, B. B., 1981: An Analysis of Wangara Micrometeorology: Surface Stress, Sensible Heat, Evaporation, and Dewfall. NOAA Tech. Memo., ERL ARL-104, Air Resources Laboratory, Silver Spring, MD, 36 pp.

Jaeger, L., 1976: Monatskarten des Niederschlags für die Ganze Erde, *Ber. Dtsch. Wetterdienstes*, **18**, 38 pp.

Kasten, F., 1977: Daily and Yearly Time Variation of Solar and Terrestrial Radiation Fluxes as Deduced from Many Years Records at Hamburg. *Solar Energy*, **19**, 589-593.

Kessler, A., 1985: *General Climatology, 1A: Heat Balance Climatology.* O.M. Essenwanger, Ed., Elsevier, 224 pp.

Kowalczyk, E.A., Garratt, J.R., Krummel P.B., 1991: A Soil-Canopy Scheme for Use in a Numerical Model of the Atmosphere - 1D Stand-Alone Model, CSIRO Div. Atm. Res. Technical Paper No. 23, 56 pp.

Lacis, A. A., and J. E. Hansen, 1974: A Parameterization for the Absorption of Solar Radiation in the Earth's Atmosphere. *J. Atmos. Sci.*, **31**, 118-133.

Legates, D. R., and C. J. Willmott, 1990: Mean Seasonal and Spatial Variability in Global Surface Air Temperature. *Theor. Appl. Climatol.*, **41**, 11-21.

Legates, D. R., and C. J. Willmott, 1992: A Comparison of GCM-Simulated and Observed Mean January and July Precipitation. *Palaeogeogr., Palaeoclim., and Palaeoecol.*, **97**, 345-363.

Louis, J.F., 1979: A Parametric Model of Vertical Eddy Fluxes in the Atmosphere. *Bound. Layer Meteor.*, **17**, 187-202.

McGregor, J.L., Gordon, H.B., Watterson, I.G., Dix, M.R., Rotstayn, L.D., 1993: The CSIRO 9-level Atmosperic General Circulation Model, CSIRO Div. Atm. Res., Technical Paper No. 26, 89 pp.

Noilhan, J. and S. Planton, 1989: A Simple Parameterization of Land Surface Processes for Meteorological Models. *Mon. Wea. Rev.*, **117**, 536-549.

Posey, J.W. and P.F. Clapp, 1964: Global Distribution of Normal Surface Albedos. *Geofis. Int.*, **4**, 33-49.

Rikus, L., 1990: The Response of the BMRC Global Model to Uniform Changes in Sea-Surface Temperatures. BMRC Research Report 21, Bureau of Meteor., Melbourne, 13-17.

Sato, N., Sellers, P.J., Randall, D.A., Schneider, E.K., Shukla, J., Kinter, J.L. III, Hou, Y-T. and E. Albertazzi, 1989: Effects of Implementing the Simple Biosphere Model in a General Circulation Model. *J. Atmos. Sci.*, **46**, 2757-2782.

Schwarzkopf, M.D., and S.B. Fels, 1991: The Simplified Exchange Method Revisited: An Accurate, Rapid Method for Computation of Infrared Cooling Rates and Fluxes, *J. Geophys. Res.*, **96**, 9075-9096.

Shuttleworth, W.J., 1988: Evaporation from Amazonian Rainforest. *Proc. Roy. Soc. London*, **B233**, 321-346.

Slingo, J.M., 1987: The Development and Verification of a Cloud Prediction Scheme for the ECMWF model. Quart. *J. Roy. Meteor. Soc.*, **113**, 889-927.

Warrilow, D.A., Sangster, A.B. and A. Slingo, 1986: Modelling of Land Surface Processes and their Influence on European Climate, Dynamic Climatology Tech. Note No. 38. Meteorological Office, MET O 20, Bracknell, Berks, 94 pp.

Willmott, C.J., Rowe, C.M., Mintz, Y., 1985: Climatology of the Terrestrial Seasonal Water Cycle, *J. Climatol.*, **5**, 589-606.

World Climate Disc, 1992: *Global Climatic Change Data.* Chadwyck-Healey, 2 installation discs, 1 user manual, 1 data reference guide.

CSIRO DIVISION OF ATMOSPHERIC RESEARCH TECHNICAL PAPERS

No. 1 Galbally, I. E.; Roy, C. R.; O'Brien, R. S.; Ridley, B. A.; Hastie, D. R.; Evans, W. J. F.; McElroy, C. T.; Kerr, J. B.; Hyson, P.; Knight, W.; Laby, J. E.
Measurements of trace composition of the Austal stratosphere: chemical and meteorological data. 1983. 31 p.

No. 2 Enting, I. G.
Error analysis for parameter estimates from constrained inversion. 1983. 18 p.

No. 3 Enting, I. G.; Pearman, G. I.
Refinements to a one-dimensional carbon cycle model. 1983. 35 p.

No. 4 Francey, R. J.; Barbetti, M.; Bird, T.; Beardsmore, D.; Coupland, W.; Dolezal, J. E.; Farquhar, G. D.; Flynn, R. G.; Fraser, P. J.; Gifford, R. M.; Goodman, H. S.; Kunda, B.; McPhail, S.; Nanson, G.; Pearman, G. I.; Richards, N. G.; Sharkey, T. D.; Temple, R. B.; Weir, B.
Isotopes in tree rings. 1984. 86 p.

No. 5 Enting, I. G.
Techniques for determining surface sources from surface observations of atmospheric constituents. 1984. 30 p.

No. 6 Beardsmore, D. J.; Pearman, G. I.; O'Brien, R. C.
The CSIRO (Australia) Atmospheric Carbon Dioxide Monitoring Program: surface data. 1984. 115 p.

No. 7 Scott, John C.
High speed magnetic tape interface for a microcomputer. 1984. 17 p.

No. 8 Galbally, I. E.; Roy, C. R.; Elsworth, C. M.; Rabich, H. A. H.
The measurement of nitrogen oxide (NO, NO_2) exchange over plant/soil surfaces. 1985. 23 p.

No. 9 Enting, I. G.
A strategy for calibrating atmospheric transport models. 1985. 25 p.

No. 10 O'Brien, D. M.
TOVPIX: software for extraction and calibration of TOVS data from the high resolution picture transmission from TIROS-N satellites. 1985. 41 p.

No. 11 Enting, I. G.; Mansbridge, J. V.
Description of a two-dimensional atmospheric transport model. 1986. 22 p.

No. 12 Everett, J. R.; O'Brien, D. M.; Davis, T. J.
A report on experiments to measure average fibre diameters by optical fourier analysis. 1986. 22 p.

No. 13 Enting, I. G.
A signal processing approach to analysing background atmospheric constituent data. 1986. 21 p.

No. 14 Enting, I. G.; Mansbridge, J. V.
Preliminary studies with a two- dimensional model using transport fields derived from a GCM. 1987. 47 p.

No. 15 O'Brien, D. M.; Mitchell, R. M.
Technical assessment of the joint CSIRO/Bureau of Meteorology proposal for a geostationary imager/ sounder over the Australian region. 1987. 53 p.

No. 16 Galbally, I. E.; Manins, P. C.; Ripari, L.; Bateup, R.
A numerical model of the late (ascending) stage of a nuclear fireball. 1987. 89 p.

No. 17 Durre, A. M.; Beer, T.
Wind information prediction study: Annaburroo meteorological data analysis. 1989. 30 p. + diskette.

No. 18 Mansbridge, J. V.; Enting, I. G.
Sensitivity studies in a two- dimensional atmospheric transport model. 1989. 33 p.

No. 19 O'Brien, D. M.; Mitchell, R. M.
Zones of feasibility for retrieval of surface pressure from observations of absorption in the A band of oxygen. 1989. 12 p.

No. 20 Evans, J. L.
Envisaged impacts of enhanced greenhouse warming on tropical cyclones in the Australian region. 1990. 31 p. [Out of print]

No. 21 Whetton, P. H.; Pittock, A. B.
Australian region intercomparison of the results of some general circulation models used in enhanced greenhouse experiments. 1991. 73 p. [Out of print]

No. 22 Enting, I. G.
Calculating future atmospheric CO_2 concentrations. 1991. 32 p.

No. 23 Kowalczyk, E. A.; Garratt, J. R.; Krummel, P. B.
A soil-canopy scheme for use in a numerical model of the atmosphere — 1D stand- alone model. 1992. 56 p.

No. 24 Physick, W. L.; Noonan, J.A.; McGregor, J.L.; Hurley, P.J.; Abbs, D.J.; Manins, P.C.
LADM: A Lagrangian Atmospheric Dispersion Model. 1994. 137 p.

No. 25 Enting, I. G.
Constraining the atmospheric carbon budget: a preliminary assessment. 1992. 28 p.

No. 26 McGregor, J. L.; Gordon, H. B.; Watterson, I. G.; Dix, M. R.; Rotstayn, L. D.
The CSIRO 9-level atmospheric general circulation model. 1993. 89 p.

No. 27 Enting, I. G.; Lassey, K. R.
The CSIRO 9-level atmospheric general circulation model. with appendix by R. A. Houghton. 1993. 42 p.

No. 28 [Not published]

No. 29 Enting, I. G.; Trudinger, C. M.; Francey, R. J.; Granek, H.
Synthesis inversion of atmospheric CO_2 using the GISS tracer transport model. 1993. 44 p.

No. 30 O'Brien, D. M.
Radiation fluxes and cloud amounts predicted by the CSIRO nine level GCM and observed by ERBE and ISCCP. 1993. 37 p.

No. 32 Kowalczyk, E.A.; Garratt, J.R.; Krummel, P.B.
Implementation of a soil-canopy scheme into the CSIRO GCM — regional aspects of the model response